CODEN:LUTEDX/(TEIE-5365)/1-98/(2015)

Industrial Electrical Engineering and Automation

GIC immune transformers

An evaluation of their GIC elimination and fault behaviour

Kajsa Eriksson Rosenkvist

Division of Industrial Electrical Engineering and Automation
Faculty of Engineering, Lund University

Abstract

Geomagnetically Induced Currents (GICs) arise from fluctuations in Earths magnetic field and can reach alarmingly high levels and cause malfunctions or blackouts in the power grids in which they occur. AF Klercker Alaküla and Lindahl invented a patented GIC immune transformer which eliminates the effects of GICs, though it is not known how this implementation will affect the transformers behavior during un-symmetrical faults. This project aims to clarify the impact of the patented implementation, with regard to fault current and voltage rise at single-line-to-ground faults, as well as verify the beneficial effects on GICs. Experiments on lab transformers corresponding to the specifications in the mentioned patent and simulations of a full scale equivalent were performed. Both the experiment and simulation results show that the GIC immune transformer eliminates the effects of GIC. The simulations also indicate that the fault current, of a bolted single-line-to-ground fault, is increased, and the voltages decreased, by replacing a regular transformer with the patented implementation. For unaltered current and voltages a grounding reactance can be used. The work shows that such a reactance should be the sum of the uncompensated grounding reactance and one third of the transformers uncompensated zero-sequence reactance.

Acknowledgments

This thesis would not have been possible if it had not been for the help and support provided by the supervisor, Olof Samuelson, and the examinator, Johan Björnstedt. The author would also like to thank Sture Lindahl, Peter Wintoft and the employees at IEA in general for answering questions and providing ideas when needed. A special thanks goes out to Getachew Darge for helping with material and equipment through out the whole process.

Contents

List of Acronyms

AC Alternating Current

AE Auroral Electrojet

CME Coronal Mass Ejection

COG Coefficient Of Grounding

DC Direct Current

DFT Discrete Fourier Transform

Dst Disturbance storm time

FDR Frequency Distribution of Reference

FMI Finnish Meteorological Institute

GIC Geomagnetically Induced Current

GMD Geomagnetic Disturbance

IAGA International Association of Geomagnetism and Aeronomy

ICME Interplanetary Coronal Mass Ejection

IMF Interplanetary Magnetic Field

MHD Magnetohydrodynamic

NI National Instruments

p.u. Per unit

rms Root-mean-square

List of Symbols

B Magnetic flux density

D Electric displacement of magnetic flux density

E Nominal line-to-neutral voltage

H Horizontal component of the magnetic flux density

I_0 Zero-sequence current

I_1 Positive-sequence current

I_2 Negative-sequence current

I_{base} per unit current base

I_{DC} Direct Current current

I_F Fault current

$I_{3\Phi}$ Three-phase short-circuit current

I_{NL} No-load current

I_{SC} Short-circuit current

k Impedance ratio

L_l Leakage inductance

L_m Magnetization inductance

n Coefficient used with positive-sequence reactance in zero-sequence impedance

P Active power

P_{NL} No-load active power

P_{SC} Short-circuit active power

Q Reactive power

R_0 Zero-sequence resistance

R_1 Positive-sequence resistance

R_{DC} Direct Current resistance

R_m Magnetization resistance

R_N Neutral point resistance

R_{ON} On resistance

R_w Winding resistance

S_{base} per unit power base

U_0 Zero-sequence voltage

U_1 Positive-sequence voltage

U_2 Negative-sequence voltage

U_{base} per unit voltage base

U_{DC} Direct Current voltage

U_f Forward voltage

U_{LG} Line-to-ground voltage

U_{LL} Line-to-line voltage

U_{LN} Line-to-neutral voltage

U_{max} Maximum line-to-ground voltage during fault

U_{NL} No-load voltage

U_{SC} Short-circuit voltage

v_A Alfvénic velocity

X_0 Zero-sequence reactance

X_1 Positive-sequence reactance

X_N Neutral point reactance

Z_0 Zero-sequence impedance

Z_1 Positive-sequence impedance

Z_2 Negative-sequence impedance

Z_{base} per unit impedance base

Z_{comp} Compensation impedance

Z_F Fault impedance

Z_N Neutral point impedance

ϕ Magnetic flux

Φ_{base} per unit magnetic flux base

Chapter 1

Introduction

1.1 Background

Geomagnetically Induced Currents (GICs) arise in the power grid when the earth's magnetic field varies due to fluctuations in the solar radiation stream passing the earth's atmosphere. These currents have a very low frequency and are thus viewed as Direct Currents (DCs). As the currents are very large they can cause malfunctions in said power grid and lead to regional blackouts, [2].

Blackouts of these sizes are not just inconvenient they can also incur large costs and risk to society. These consequences are the reason that a number of different government agencies from multiple nations are so interested in finding a way to protect their equipment from GICs, primarily from the half cycle saturation they bring on. One way of achieving this is found in the patented invention of Professor Mats Alaküla and Professor Sture Lindahl, the GIC immune power transformer, [1].

There is a number of different transformers on the market today and the effects of using the GIC immune implementation on these differ. Though the new design is insensitive to GICs the effects of fault currents and voltages due to asymmetrical faults have not been analyzed. How efficient are the compensation windings in the GIC immune transformer? Are there differences between core types, configurations or GIC representation?

In Finland the transformers are grounded through an impedance which incidentally protects against GICs, [3]. The sizing of this impedance is a trade-off between reducing fault currents and reducing voltages during fault. Does the patented implementation make it possible to use a smaller impedances and still get the same performance in respect to the fault current and voltage?

1.2 Purpose

This project is to continue the evaluation of the GIC immune power transformer started by Olof Samuelsson and described in his article, Power Transformer Immune to GICs [4]. It aims to clarify the impact of the GIC immune power transformer construction and investigate the pros and cons in comparison to the Finnish implementation, which has not been done before.

1.3 Assignment

The assignment will consist of experiments and simulations. In the first part the single-phase-, the three-phase three-legged- and the three-phase five-legged transformer will be evaluated, with respect to asymmetrical faults and GICs, with and without the GIC immune implementation. During these evaluations the load will be held constant and the power supply altered to prevent currents or voltages from exceeding the nominal values. In examining the fault behavior the GIC will be zero while the GIC tests are performed without fault. The parameters for the grounding impedance and resistance will be varied and measurements taken for a number of values as well as for direct and ungrounded neutral points.

In the second part, investigation of the designs impact on the sizing of grounding impedance will be done by creating a SimPowerSystems model of a full scale circuit which resembles the lab setup, in this case only the single-phase transformers will be evaluated, and running simulations of GICs and faults with varying grounding impedance.

Chapter 2

Theory

This chapter covers the theory needed for this thesis. It begins by explaining Geomagnetically Induced Currents (GICs), their cause, effects and some mitigation methods. Then it continues with the explanation of unsymmetrical faults where a few scenarios are presented. This part of the chapter also covers effectively grounded systems and their fault currents and voltages.

2.1 Geomagnetically Induced Currents

GICs are currents with very low frequencies, near DC, that are induced in, among other thing, the long electric conductors of our power grids. Over 150 years ago the existence of GICs was noted in telegraph equipment and as other systems, such as power and telephone grids, developed and grew so did the presence and magnitude of GICs, [5]. The size and complexity of today's grid makes if more prone to these currents than ever before and in 2000 the largest known GIC in the world, 320 A, was recorded in the Swedish 400 kV power grid, [5].

2.1.1 Cause

Solar Storms

Though the Sun might seem like a homogeneous ball of fire to the naked eye, it actually has a complex magnetic field [6]. In the beginning of the 17th century the dark spots, sunspots, observable when studying the Sun were argued, by Christoph Schreiner, to be small planets. In 1613 Galileo Galilei showed them to be structures on the Suns surface [7]. Sunspots occur when an intense magnetic flux tube emerges from the convection zone to the photosphere. These magnetic fields can be as large as 0.3 T and they can cause spots with diameters of up to 20 000 km. By keeping the hot plasma from reaching the photosphere the magnetic field lowers the temperature from 5778 K to about 4100 K at the center of the spot and it is this relatively low temperature that is observed as a dark spot [7].

In 1844 Heinrich Schwabe showed that the sunspot activity follows an eleven year cycle and in 1852 Edward Sabine noted that so does the geomagnetic storm activity on Earth, though he did not make the connection [7, 8]. This

correlation was first suspected by Richard Christopher Carrington in 1859, when he reported that a large magnetic storm followed the great solar flare, observed by him and Richard Hodgson, that occurred in September of that year, but it was not until Harold William Newton performed a statistic survey in 1943 that it was accepted [8].

The eleven year sun cycle starts with a period of low activity called a solar minimum, the activity increases slowly to a high activity peak, solar maximum, that lasts for a few years after which the activity decreases again and the cycle ends with low activity [6]. In 1923 George Ellery Hale confirmed that the magnetic orientation of connected sunspots, leader and follower, remains the same over the whole eleven year cycle and the polarity reverses from one cycle to the next, that is the Suns magnetic cycle spans over 22 years [7]. The odd-numbered sun cycles are, as a rule, more severe then the even-numbered cycle they follow and there are some indications that the solar storm activity is increasing over all [2].

The changes in the Suns magnetic field are essential in the creation of space weather. The solar wind, the stream of plasma escaping the Sun, is divided into two main categories, a tenuous and fast, about 750 km s^{-1}, and a dense and slow, about 350 km s^{-1}. Though it is not yet confirmed the general view is that large coronal holes at high solar latitudes give rise to the fast solar wind while the slow wind originates from smaller and less permanent structures at lower latitudes. A third type of solar wind is the outflow related to Coronal Mass Ejections (CMEs) and in addition to these the varying magnetic field also gives rise to solar flares [7].

A solar flare is a process where the Sun releases up to 10^{25} J, at a total power of about $10^{20} - 10^{22}$ W, in about 10 minutes or less. This might seem unbelievable but when considering that coronal loops, magnetic flux tubes filled with plasma that reaches out to the corona, can reach about 6×10^{25} J, for a radius of 20 000 km and a length of 100 000 km, it is very reasonable. The energy emitted in a solar flare is primarily in the form of electromagnetic radiation with a wide spread angle.

CMEs are large magnetic plasma clouds leaving the Suns lower atmosphere through the corona. As the total kinetic energy in a CME is about $10^{24} - 10^{25}$ J it seems, in respect to energy emission, similar to solar flares. However, contrary to flares the energy in a CME is mostly mass, about $5 \times 10^{12} - 5 \times 10^{13}$ kg. As a CME moves away from the Sun it is referred to as an Interplanetary CME (ICME). Though both CMEs and solar flares are of great importance to space storms the mass flux of ICMEs and their powerful magnetic field implies that they have a much greater impact on Earths magnetosphere than flares have. ICMEs are, along with the fast solar wind, the main drivers of magnetospheric storms. It is in fact the ICMEs that are the most important driver of solar wind shocks and depending on the orientation and structure of the system they cause the most severe magnetic storms on Earth.

Not all ICMEs are capable of driving a shock ahead of them. To do this it must have a velocity which is super-Alfvénic in reference to the surrounding plasma flow. That is, the velocity must be greater than the Alfvénic velocity (v_A)

$$v_A = \frac{B_0}{\sqrt{\rho_m \mu_0}} \text{Vs/Am} \tag{2.1}$$

where ρ_m is the mass density and $\mu_0 = 4\pi \times 10^{-7}$ $^{\mathrm{Vs}}/_{\mathrm{Am}}$ is the vacuum permeability. Due to this slow ICMEs does not drive shocks [7]. A fast ICME is composed of three parts, the "shock", the "sheath" and the driver-gas. The shock is followed by the sheath which consists of plasma and fields from the slower stream that has been swept-up and compressed by the ICMEs and behind this is the driver-gas, see Figure 2.1, [8].

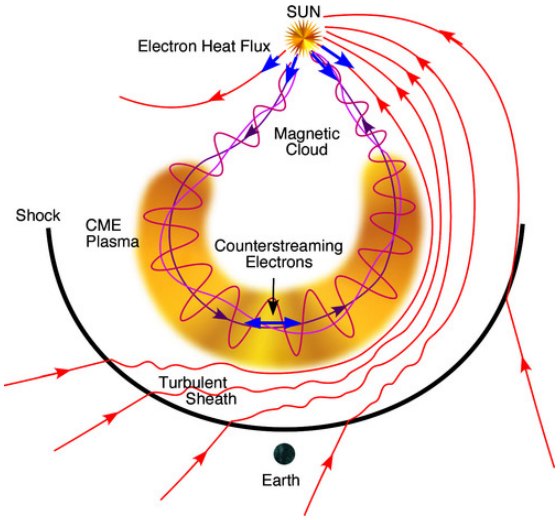

Figure 2.1: The structure of an Interplanetary CME, showing the "shock", "sheath" ("turbulent sheath") and "driver-gas" ("CME plasma" and "magnetic cloud"). Picture taken from `http://ase.tufts.edu/cosmos/print_images.asp?id=47`, 15 September 2015.

Interplanetary spacecrafts have measured high-speed plasma streams, rich in helium, in association with intense solar flares. These speed changes identify the solar ejecta and in combination with coronograph images of ICMEs the plasma link between the Sun and the Earth is established [8].

Geomagnetic Disturbances

The Earth has its own internal magnetic field, the geomagnetic field, that deflects the charged solar wind particles round the magnetosphere. Except for its innermost regions, the ionosphere and the plasmasphere, the magnetosphere is a magnetic cavity surrounding the planet and, as for all the magnetic planets, it protects the atmosphere, without which life would not be possible, from being striped away by the solar wind[7, 8].

As the geomagnetic field is exposed to solar wind rushing by, it is contorted. The dayside field is compressed and on the nightside the field is stretched out to a long tail. The Magnetohydrodynamic (MHD) plasma in the magnetosphere resists blending with that in the solar wind and a current layer, called the magnetopause, is formed to protect the magnetic field. The stretching of the long tail calls for a similar current inside the magnetosphere. In the ideal representation of the geomagnetic field there is, unavoidably, two points of zero magnetic

field on the magnetopause. These points are magnetically connected to Earths auroral regions through regions called polar cusps. These regions allow solar wind plasma to flow directly to the ionosphere and ionospheric plasma to enter the solar wind [7].

In comparison to the Earth, the solar wind travels at super-Avlfvénic velocity and due to this a collisionless shock front, called the bow shock, is formed ahead of the magnetosphere and between this and the magnetopause is a region called the magnetosheath [7].

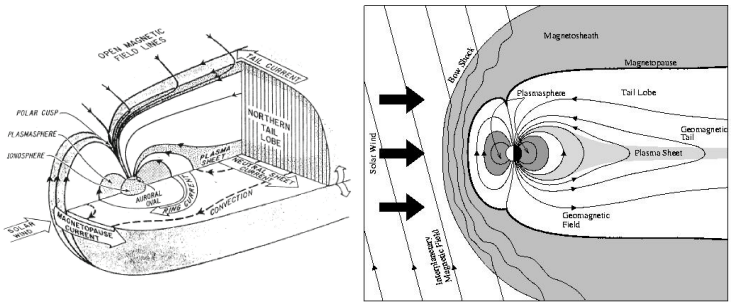

(a) Picture from `http://www.phy6.org/Education/JAS1.htm`.

(b) Picture from `http://www.tp.umu.se/forskning/space/`.

Figure 2.2: Schematic representations of the Earths magnetosphere. Pictures taken from the sites 15 September 2015.

Reconnection is one of the most important concepts when studying space storms as it is involved in solar flares, CME detachment, the interaction between solar wind and magnetosphere and substorm onsets. The most general view on this is described by considering plasma floating in space without colliding. Plasma elements on the same magnetic field line are magnetically connected to each other and continue to be so just as unconnected elements continue to be free. When this connectivity changes, either by free elements attaching to the field or some of the connected elements breaking of, a reconnection literary occurs. Though the physical microscopic mechanism behind this process is not yet known it is clear, from empirical studies, that reconnections can be explosive both in solar flares and substorm onsets [7].

Magnetic reconnection is most efficient when the fields are of opposite directions and thus Interplanetary Magnetic Fields (IMFs) with southward orientation cause the most powerful reconnections. When an IMF penetrates the bow shock and magnetosheath it can come in contact with the dayside terrestrial field lines and cause reconnection. The reconnected field line is then dragged to the nightside by the solar wind. In this process a dayside line inside the magnetosphere is converted to a nightside tail line leading to an accumulation of magnetic flux which pushes the inner lines closer and closer to the cross-tail current sheet. About $100-200$ Earth radii from Earth the lines are so close that they reconnect across the current sheet and the terrestrial field line is pulled toward Earths midnight line. Since the returning flow is not able to penetrate the corotating plasmasphere it is forced to go around Earth to the dayside, dragging the ionospheric end of the field line along the dawn or dusk side of the auroral

region, see Figure 2.3 [7].

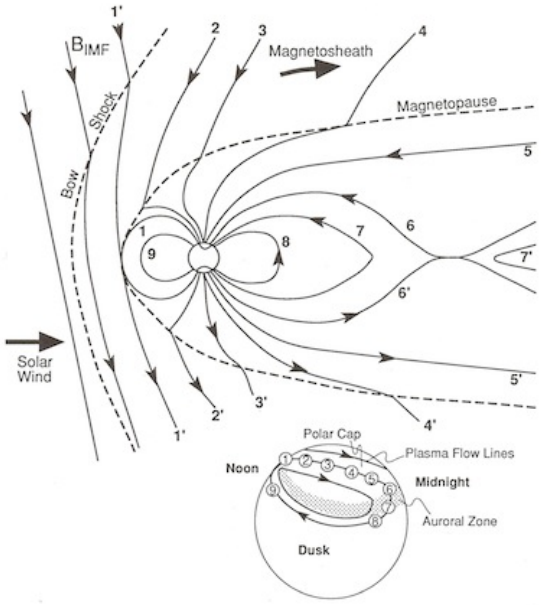

Figure 2.3: The magnetic reconnection process which occurs when an Interplanetary Magnetic Field interacts with the Earths geomagnetic field. Picture taken from `http://inspirehep.net/record/1283584/plots`, 15 September 2015.

A steady-state convection may arise if the dayside and nightside reconnections occur at with the same rate but the magnetospheric response to the changes in the solar wind are usually faster than the nightside to dayside circulation. Due to this the dayside magnetic field may be significantly eroded and the changes in the tail magnetic flux cause the polar cusps to expand and contract [7].

The fluctuations in the ionosphere and currents induced in Earth cause potential differences in the ground which drives currents through man made structures, e.g. pipes or power conductors [2]. These currents are what is called GICs. Since the electric field increases with higher latitude these regions experience higher amounts of GIC and due to this most of the research in this field, in Europe, is done in Sweden and Finland [5]. The GIC increases with the length of the conductor and endpoints are especially prone to the phenomenon.

Severity of Geomagnetic Disturbances In order to be prepared to handle the effects of a Geomagnetic Disturbance (GMD) utilities require reliable forecasts that predict when the storm will start and end as well as which regions that are to be affected and the severity of the storm. While satellites in low orbit track the location and structure of the ionospheric current higher orbit satellites measure the density, polarity and velocity of the solar wind and this data is used in the attempt to determine this information [2].

The severity of a GMD can be measured in several ways and the officially recognized, by International Association of Geomagnetism and Aeronomy (IAGA),

indices are grouped into three categories, range indices, planetary indices derived from them and AE and Dst indices. The different indices have different strengths and weaknesses, e.g. a planetary index can not be used to identify particularly exposed regions but is insensitive to small-scale disturbances [9].

The K index is a local range index that is derived from the larger range of the irregular variations obtained in the two components, horizontal component of the magnetic flux density (H) or electric displacement of magnetic flux density (D), over a 3 hour interval. This value is ranked into one of the range classes that corresponds to $K = 0, 1, \ldots 9$. Since the scale is not linear it is often referred to as quasi-logarithmic. Each observatory has its own successive steps where the index increases faster for lower indices than for higher ones but they do not follow a true logarithmic curve [2, 9].

The K_p index is obtained by standardizing the K indices from a certain network of observatories, using a specific Frequency Distribution of Reference (FDR). This gives a planetary index that, just like the K index, is a 3 hour index with a quasi-logarithmic scale. The index ranges from 0 to 9 but in thirds and is written as $K_p = 0_0, 1_-, 1_0, 1_+, \ldots 9_-, 9_0$ [9]. From the K index it is also possible to derive a daily index called the A_k index that ranges from $0 - 400$ and is based on 8 consecutive $K-$values [2].

The Auroral Electrojet (AE) index is a 2.5 minute or hourly index which is measured in nT. For a certain network of auroral stations the $AE = AU - AL$, where AU is the upper and AL is the lower envelope between which the H curves of all stations lie. The index is independent of any existing zonal currents in the ionosphere and depends solely on the maximum eastward, $\Delta H > 0$, and westward, $\Delta H < 0$, electrojet currents [9].

The Disturbance storm time (Dst) index is an hourly index that mainly relates to the ring current. It is the average of H measured at the observatories in Hermanus, Kakioka, Honolulu and San Juan. A negative value indicates that Earth's magnetic field is weakened which is the case during a solar storm. Higher negative-values correspond to more severe storms and events with values of less than -500 nT are defined as intense geomagnetic storms [9, 10].

When the K index value is between $0 - 4$ we have what is called quiet geomagnetic activity. This corresponds to A_k values of $0-7$. During a minor storm $K = 5$ and A_k is in the range $30 - 50$ and for a severe storm the corresponding values are $7 - 9$ and $100 - 400$ respectively. However convenient these indices are they do not translate to GIC values for which the time derivative of the magnetic flux density (B) over seconds or minutes is more important [2].

2.1.2 Effect

The effects of GICs in a power system depend on a number of variables, not only the length of the power lines and the position, geographical and in the system. Studies have shown that the choice of transformer type is critical since single-phase transformers are more sensitive than three-phase transformers, also the five-leg configuration is more susceptible than the three-leg one and shell transformers are more sensitive than core transformers [2]. The Finnish and Swedish utilities prefer different transformer types which is likely a contributing factor in the reason why Finland has not suffered the same extent of the effects that Sweden has [5].

The GIC is typically the same in all three phases during a GMD and thus cause a zero-sequence-like current (I_0), see Appendix A, in the transformer. If the winding are connected in delta configuration the GIC induces a circulating current which prevents the core from penetrating the near DC flux and this means that the transformer saturation and the reactive power loss is decreased [11].

Since GICs have very low frequencies, 0.1 mHz-0.1 Hz [12], they are thought of as Direct Currents (DCs) that offset the Alternating Currents (ACs) in one direction and thus cause half-cycle saturation, see Figure 2.4. Half-cycle saturation causes nonlinear operation of the transformer and large asymmetric exciting currents that leads to an enhanced content of harmonics [5]. The increase in harmonic magnitude is somewhat proportional to the GIC though for very large GIC values the contribution of harmonics decline[2]. During normal operation even harmonics are not expected in the system, which therefore is not designed to handle them, but when the harmonic content increases the system is exposed to e.g. the negative-sequence 2nd order harmonic which causes generator heating [2]. Saturation, or half-cycle saturation, of transformers force the magnetic flux to take paths that they were not intended to, e.g. through the tank which is heated by the resulting eddy currents [4]. This puts the transformer at risk of failure and can even cause permanent damage [13, p. 4].

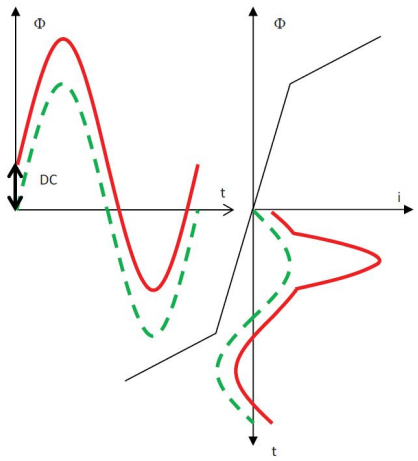

Figure 2.4: Magnetic flux and current in a typical transformer with hysteresis neglected during normal, dashed, and half-cycle saturated operation, solid. Picture taken from [4]

As the GIC is identical in all three phases it gives rise to a I_0 that can result in significant neutral currents at locations where it is usually very small [2]. This can cause false tripping of neutral over-current relays and similarly other protective relays can be tripped due to the voltage fluctuations that can occur, especially if the neutral is not directly grounded [5]. Other problems connected with the asymmetric exciting current are e.g. increased reactive power losses and as a result of the combination of some of these problems the system can ultimately collapse, like it did in Malmö, Sweden, in 2003, due to an abnormal

switching state combined with false over-current relay tripping [5].

2.1.3 Mitigation Methods

Since 1977, Finnish Meteorological Institute (FMI) have monitored GICs in the nations high-voltage power grid [5]. Most of the recordings are done on the 400 kV system and though some measurements have been made on the line currents most are of neutral point currents. The largest of these neutral point currents measured 201 A and was recorded in Rauma in 1991 [5]. Though values this high have been encountered, Finland has never experienced outages or equipment malfunctions or failures caused by GICs [14]. In 1979 and 1999 field tests were done and saturation effects like phase-current distortion and increased temperatures were observed, though based on modeled statistics of GIC occurrence, it was concluded that the probability of serious problems was very low however the research and monitoring was to continue [5, 14].

Blocking and Suppressing Devices

The Finnish high-voltage power grid is somewhat protected from the harmful effects of GICs thanks to the fact that series capacitors and neutral reactors are common in Finland. Though it is not their primary function they act as blocking or suppressing devices to the GIC, [2, 3, 5]. These mitigation methods are dependent on the number of devices used and their placement in the system since installing a device at one point will result in the re-distribution of the GIC across the system, though there is a limit to the distance [2, 15]. Zhu and Overbye discuss the difficulties in placing these devices and notes the inter-dependencies between transformer nodes in the system which makes the process of finding optimal placement an iterative one [15].

Series Capacitance Conventionally, series capacitors are installed in each phase of a transmission line to increase its power transfer capability [2, 4]. While AC flows quite easily through these capacitors the near DC GICs are blocked which is a most welcome side effect. Capacitors used for power increasing reasons are costly and installing them for the sole purpose of blocking GICs is not economically viable. One could instead install capacitors specifically developed for GIC blocking which are less costly due to their much lower capacitance [2].

Grounding Reactance Installing a capacitor between the neutral point of a transformer and ground does not effect the power transfer capability but when GIC blocking is concerned it works similarly to series capacitors [2]. Due to their DC resistance, which is typically two to four times larger than the sum of the systems other resistances, they suppress the GIC flow, [3]. An advantage of using a grounding capacitor instead of series capacitors is that one only needs one third the quantity though since the current in the neutral is three times that in each phase it is possible that a different size of capacitor would be needed in this configuration.

Using a capacitance means that the impedance is much lower, almost short-circuited, for the AC than for the near DC GICs. Though using an inductor instead of a capacitor will result in a higher impedance for the AC than for the DC, which has its advantages, the GIC will still be suppressed if the inductor

has a sufficiently high DC resistance, a few Ωs is all that is needed since this is significant in relation to the DC impedance of the system.

Grounding Resistance If the frequency dependent effects of grounding reactors are not desired it is possible to attain the same GIC suppressing properties using a resistance as with an inductor, provided that they have the same DC impedance.

Installing a sufficient number of blocking devices to achieve complete protection is very costly and therefore utilities often use GIC system operation guidelines [2]. This means that a set of guidelines for measures to be taken when notified of an oncoming GMD is drawn up. Choosing what level of threat makes a certain measure necessary is very difficult and the guidelines must have clear delimitation since the decisions need to be taken fast in the event of an alert as some implementations can take hours to complete. The duration of a GMD is also very hard to predict which makes the question of when to return to normal operation a problem. Connecting blocking devices, turning of shunt reactors and adjusting relay settings to counteract false tripping are some of the examples mentioned by Molinski.

GIC Immune Transformer

In a balanced ideal system the phase currents have the same magnitude and are at an 120°angle to each other which means that the I_0 and negative-sequence current (I_2) are zero and the positive-sequence current (I_1) is equal to the current in phase A. When a GIC is induced into the system the I_0 is no longer zero but three times the phase GIC. This current now flows through the neutral point to ground which the GIC immune transformer utilizes to cancel out the effects. By leading the neutral current through three compensation windings, one per phase, the DC flux is eliminated. This is made possible by giving the compensation windings one third the number of turns that the main winding and connecting them in series with opposite polarity [1, 4]. The turn ratio is based on that the neutral GIC is three times that of the phase GIC and connecting them with opposite polarity results in a DC flux that neutralizes that created by the main windings. The GIC was invented by AF Klercker Alaküla and Lindahl and their patent, [1], includes a number of configurations in which the compensation windings can be used.

2.2 Unsymmetrical Faults

2.2.1 Types of Fault

There are a number of unsymmetrical fault types including unsymmetrical short-circuits which can be bolted, have zero impedance, or have a fault impedance (Z_F). When one line short-circuits to ground it is called a single-line-to-ground fault[16]. Figure 2.6 shows the interconnected sequence networks of the system in Figure 2.5.

Short-circuits between two lines are referred to as line-to-line faults, see Figure 2.7. In accordance with Kirchhoff's voltage law, the sum of line-to-

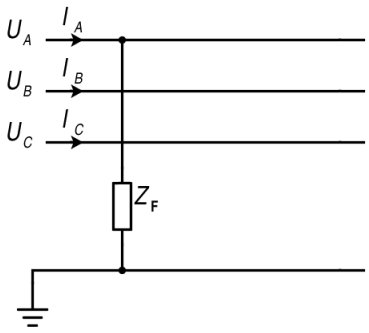

Figure 2.5: Grid representation of a single-line-to-ground fault in a three-phase system.

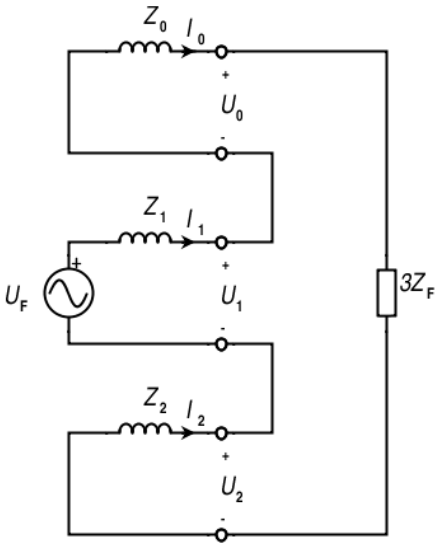

Figure 2.6: The interconnected sequence networks of the single-line-to-ground fault in Figure 2.5.

line voltages is always zero which means that their zero-sequence component, zero-sequence voltage (U_0), is zero as well and the zero-sequence network is not attached to the other sequence networks [16, 17]. The positive-sequence network and the negative-sequence network are connected through Z_F as shown in Figure 2.8.

A double-line-to-ground fault is a short-circuit between to phases and ground. In this case there are three different fault impedances as there can be one in connection with each phase involved and, once they connect, one in the earth connection, see Figure 2.9. Figure 2.10 shows the interconnected sequence networks.

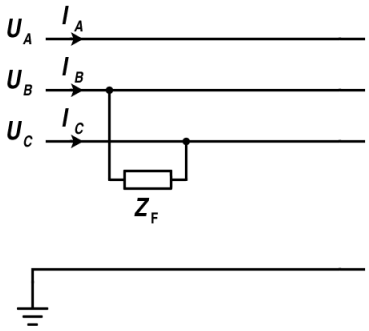

Figure 2.7: Grid representation of a line-to-line fault in a three-phase system.

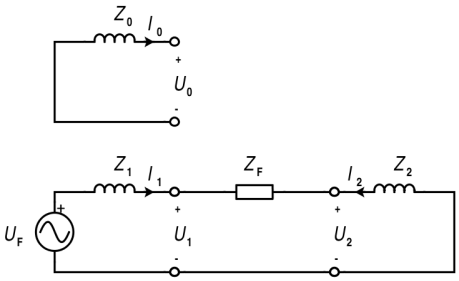

Figure 2.8: The interconnected sequence networks of the line-to-line fault in Figure 2.7

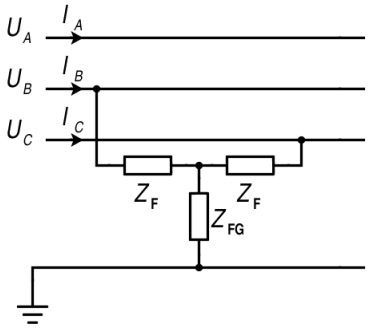

Figure 2.9: Grid representation of a double-line-to-ground fault in a three phase system.

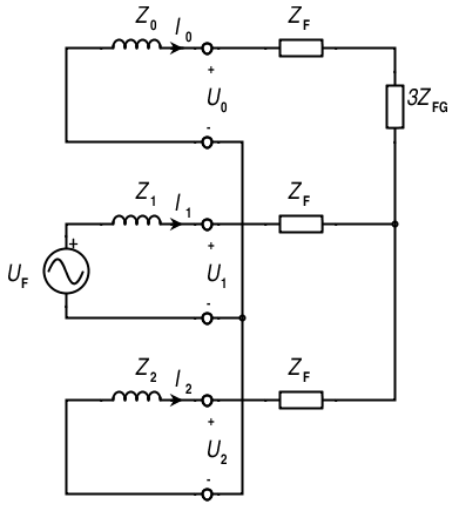

Figure 2.10: The interconnected sequence networks of the double-line-to-ground fault in Figure 2.9.

2.2.2 Grounding of Systems

In a balanced isolated system, with no connection between neutral point and ground, the stray capacitances throughout the grid keeps the three line-to-neutral voltage magnitudes at the same level. The instantaneous line-to-neutral voltages then add to zero, thus give the neutral point ground electric potential. When a bolted single-line-to-ground fault occurs in such a system the voltage in that phase, e.g. phase A, is forced to zero, [18]. This causes the neutral point voltage to be $-\overline{U_A}$, i.e. $-\hat{U_A} \times e^{i\omega t}$, and as the voltages from this point to the two other phases are unaltered they now have the magnitude $\sqrt{3}E$, where E is the nominal line-to-neutral voltage, in reference to ground, see Figure 2.11.

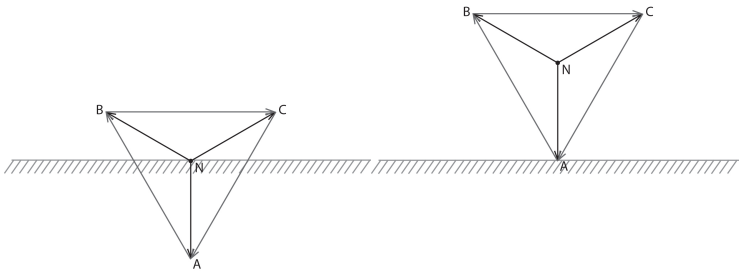

(a) Normal operation (b) Bolted single-line-to-ground fault

Figure 2.11: Complex voltage phasors in an isolated system.

For an isolated system the neutral point impedance (Z_N) is infinite, lowering this, i.e. connecting the neutral point to ground through some impedance, will affect the neutral point voltage at fault and thus altering the un-faulted line-to-ground voltages. Figure 2.12 shows a solidly grounded system at normal operation and with a bolted fault in phase A. Note that the un-faulted line-to-ground voltages are unaffected by the change in phase A voltage as this can not alter the neutral point voltage.

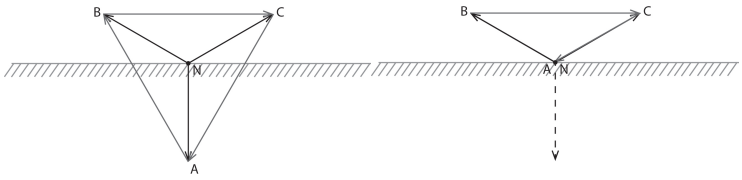

(a) Normal operation (b) Bolted single-line-to-ground fault

Figure 2.12: Complex voltage phasors in an solidly grounded system.

It is not only the size of Z_N that is of importance to this shift in neutral point. The type of impedance, resistive or reactive, determines the manner in which the neutral point voltage is altered. Figure 2.13 shows how a system is affected by inductive and resistive grounding, respectively, [19].

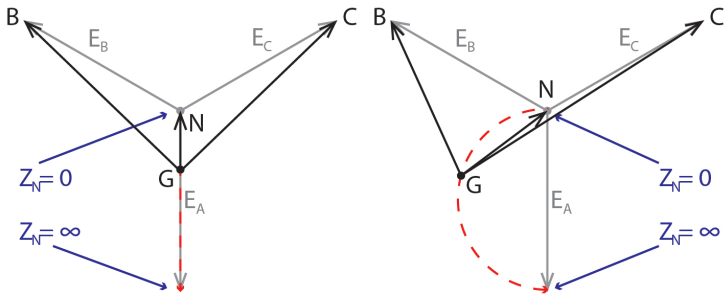

(a) Inductive grounding (b) Resistive grounding

Figure 2.13: Grounding effects on fault voltages shown as phasors.

Effectively Grounded Systems

An effectively grounded system is a system with low-impedance grounded neutrals. The voltages in an effectively grounded system are restricted by the definition that the highest fundamental frequency line-to-ground voltage in one of the sound phases, at fault (U_{LG_F}), must be lower than 140% of line-to-ground voltage (U_{LG}), before fault, independent of where the fault occurs. There is no fixed limitation of the ground fault currents (I_Fs) in an effectively grounded system but due to the voltage restrictions they have about the same magnitude as the three-phase short-circuit currents ($I_{3\Phi}$s), though they may exceed $I_{3\Phi}$, and are determined by the series impedances and the neutral point impedance [19, 20].

IEEE has defined a more restrictive standard which states that the system must be *"grounded through a sufficiently low impedance (inherent or intentionally added, or both) so that the COG does not exceed 80%"*, where the Coefficient Of Grounding (COG) is determined from the (U_{LG_F}) and the line-to-line voltage (U_{LL}) before fault according to (2.2). This is obtained if the ratio of the zero-sequence reactance (X_0) to the positive-sequence reactance (X_1) is positive and less than, or equal to, 3, ($^{X_0}/_{X_1} \leq 3$), while the ratio of the zero-sequence resistance (R_0) to X_1 is positive and less than 1, ($^{R_0}/_{X_1} < 1$), [21]. According to Pesonen et al. these restrictions might be regarded as too severe. For e.g. a 400 kV system, accounting for the actual resistances, the 140% limit can be maintained as long as the ratios $^{X_0}/_{X_1} \leq 4.5$ and $^{R_0}/_{X_1} < 1$ are not exceeded. The stricter limits result in a minimum I_F which is 60% of $I_{3\Phi}$ while 46% is obtainable when using the more liberal limits. This decrease in I_F is the reason that Finnish utilities prefer to use the higher ratio, though it results in a higher fault voltage than with the lower ratio, [22].

$$COG = 100\% \times \frac{U_{LG_F}}{U_{LL}} \tag{2.2}$$

2.2.3 Fault Currents

Figure 2.6 shows the sequence networks of a single-line-to-ground fault from which the relation in (2.3) is easily derived [16].

$$I_0 = I_1 = I_2 = I_F = \frac{U_F}{Z_0 + Z_1 + Z_2 + 3Z_F} \tag{2.3}$$

Assuming that the zero-sequence impedance (Z_0) can be freely varied and utilizing the fact that $I_{3\Phi}$ does not depend on Z_0 the relation between I_F and the sequence impedance ratio can be calculated if Z_F is known. For a power transformer it is customary to assume $Z_1 = 0.0995 + 0.995i$ per unit (p.u.) when the actual value is not known and this is utilized here, [23]. For stationary units, such as transformers, the negative-sequence impedance (Z_2) is equal to positive-sequence impedance (Z_1), [24]. In Figure 2.14 R_0 and X_0 are varied independently and the resulting I_F using X_0 (y-axis) and R_0 (x-axis) is shown for a bolted, $Z_F = 0$, fault. Figure 2.15 shows how I_F varies when R_0 or X_0 is tuned while the other is zero. Here $k = {}^{Z_0}/_{X_1}$ and in this case the impedance ratio (k) is the same as the coefficient used with X_1 in Z_0 (n). The light grey area in Figure 2.14 marks the values included by the ${}^{X_0}/_{X_1} \leq 3, {}^{R_0}/_{X_1} < 1$ ratios and the dark grey area marks the additional values included by the ${}^{X_0}/_{X_1} \leq 4.5, {}^{R_0}/_{X_1} < 1$ ratios. In Figure 2.15 these colors show the obtainable I_Fs for the same restrictions, note that no attention is paid to the ratio, k, in this graph. A black cross, $\times$, marks the point where the 60% level intersects with the completely reactive curve and a magenta circle, $\circ$, marks the corresponding point for the resistive curve.

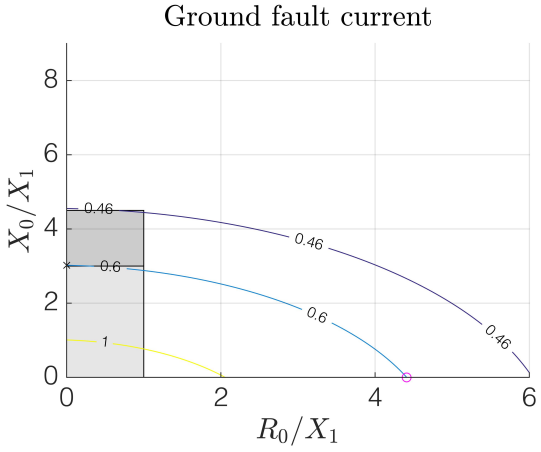

Figure 2.14: fault current to three-phase short-circuit current ratio, $I_F/I_{3\Phi}$, levels for combinations of R_0/X_1 and X_0/X_1 during a bolted single-line-to-ground fault.

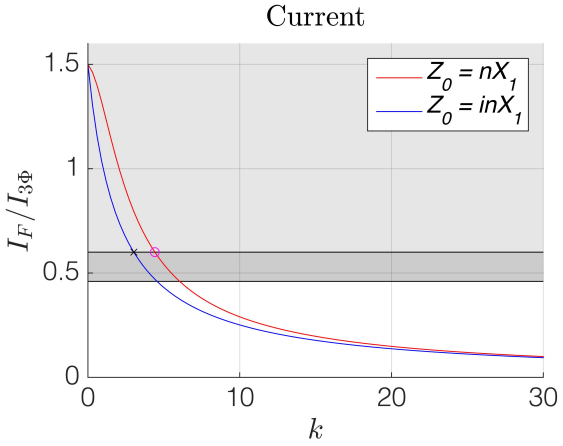

Figure 2.15: fault current to three-phase short-circuit current ratio, $I_F/I_{3\Phi}$, for different grounding resistances, red, or reactances, blue, during a bolted single-line-to-ground fault. n is the coefficient used with X_1 in Z_0 and k is impedance ratio, ${}^{Z_0}/_{X_1}$.

2.2.4 Voltage During Fault

The expressions in (2.4) and (2.5) are derived from the sequence networks of the single-line-to-ground fault, see Figure 2.6 [16].

$$U_0 + U_1 + U_2 = 3Z_F I_1 \tag{2.4}$$

$$\begin{bmatrix} U_0 \\ U_1 \\ U_2 \end{bmatrix} = \begin{bmatrix} 0 \\ U_F \\ 0 \end{bmatrix} - \begin{bmatrix} Z_0 & 0 & 0 \\ 0 & Z_1 & 0 \\ 0 & 0 & Z_2 \end{bmatrix} \begin{bmatrix} I_0 \\ I_1 \\ I_2 \end{bmatrix} \tag{2.5}$$

Utilizing this and the assumptions made in subsection 2.2.3 the sound line-to-ground voltage were calculated. Figure 2.16 shows the maximum line-to-ground voltage during fault (U_{max}) level when varying R_0 and X_0 independently and Figure 2.17 shows the sound line-to-ground voltage, phase B, C and the maximum by the dotted, dashed and solid lines respectively, when only one parameter is modified at a time. As k increases the ground point, G, in Figure 2.13 moves along the dashed red line from $Z_N = 0$ towards $Z_N = \infty$. The difference in these curves is due to the neutral point traveling, see subsection 2.2.2. As in Figure 2.14, the light grey area in Figure 2.16 marks the values included by the ${}^{X_0}/_{X_1} \leq 3, {}^{R_0}/_{X_1} < 1$ ratios and the dark grey area marks the additional values included by the ${}^{X_0}/_{X_1} \leq 4.5, {}^{R_0}/_{X_1} < 1$ ratios. In Figure 2.17 the light grey area shows the voltage limit which defines an effectively grounded system. As for Figure 2.15 $k = {}^{Z_0}/_{X_1}$. A black circle, $\circ$, marks the point where the 140% level intersects with the completely reactive curve and a magenta cross, $\times$, marks the corresponding point for the resistive curve.

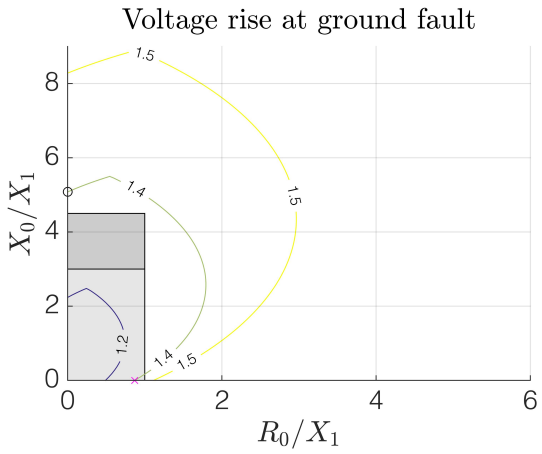

Figure 2.16: maximum line-to-ground voltage during fault to line-to-ground voltage ratio, U_{max}/U_{LG}, levels for combinations of R_0/X_1 and X_0/X_1, during a bolted single-line-to-ground fault.

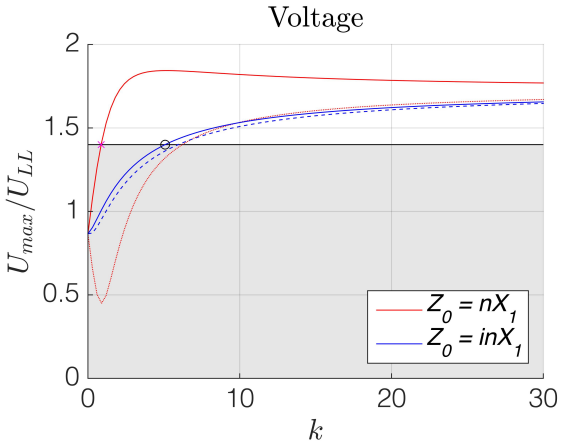

Figure 2.17: Line-to-ground voltages of the healthy phases, dashed and dotted, and their maximum, solid, for resistive, red, and reactive, blue, Z_0 during a single-line-to-ground fault.

2.3 Summary

The reasons for protecting power apparatuses from the effects of GICs are many, and so are the ways in which the protection is sought. Just as for the limiting of fault currents and voltages by determining the right Z_N, it is a deliberation to find the right mitigation method and its placement and this should not be rushed. Regarding the fault current and the sound line-to-ground voltage figures, Figure 2.15 and 2.17, it becomes apparent that since they have reversed dependencies of k, it is not possible to obtain minimal values for both fault current and sound line-to-ground voltage. Due to this a compromise to achieve sufficient suppression of both property is necessary. As this chapter demonstrates, Z_N affects the GICs as well as the fault currents and voltages and all of these must thus be taken into account when choosing the system grounding.

Chapter 3

Equipment

The equipment used during this project is presented in this chapter. Firstly the power supplies and loads are listed after which the measuring and analysis equipment is described as well as the required calibrations. This is followed by a detailed specification of the main part of the thesis, the transformers, for which a vast number of parameters have been determined.

3.1 Power Supply and Load

The main power supply in this project was a variable three-phase transformer, three mechanically connected Philips 2422 530 05411 transformers, connected to a 220 V, 50 Hz grid through an Esselte Studium 8000 053 three-phase transformer to achieve galvanic separation. In addition to this, a HQ Power PS3010 adjustable Direct Current (DC) power supply, hereafter referred to as the power box, and a 12 V car battery were used in one or more stages of the preparations and/or experiments.

In the experiment a transmission grid was modeled by three 5 mH, 20 A inductors and a three-phase three-legged 400 V/3 kVA transformer. Most measurements were taken at no load, or short circuited, but in specific cases a Terco MV1100 load resistor was used. A number of inductors and potentiometers were used in the grounding of the transformers, see Table 3.1. Some of the potentiometers were also used in adjusting the current delivered by the car battery.

Magnitude	Quantity
3 mH	3
7 mH	7
13 mH	3
22 mH	1
1 Ω	4
10 Ω	2
100 Ω	1

Table 3.1: Inductors and potentiometers used during the experiments.

3.2 Measuring Equipment

There were a number of measuring devices involved in this project. To make it possible to process the measured data in a computer, National Instruments (NI) devices, two NI 9225 units (voltage) and one NI 9239 unit (current) were used in combination with a NI cDAQ-9172 unit which provided the connection with the computer. Since the currents would have small components and the system was sensitive to DC resistances the currents were measured with current transducers wound with three turns, LEM LA50-P for the phases and LA55-P for the neutral, connected to the NI unit. Though this equipment was used for the majority of the tests it was in some cases more suitable, or even required to use other equipment. In calibrating the NI devices a Tektronix TSP 2024 oscilloscope, a Kyoritsu 8113 AC/DC current/voltage converter and an Esselte Studium 8000-771 diffprobe were used to provide the reference values, see subsection 3.2.2. Digital multimeters, MetraHit 16S, were used both in the experiment and, along with Norma D1150 wattmeters, in determining the characteristics of the transformers, see Appendix B.

3.2.1 Analysis Equipment

The NI measurements were controlled and processed by a LabView script which generated spreadsheet files, listing all samples. A sampling frequency of 2 kHz was used for all NI measurements though the measuring time varied. All measurements, both using the NI devices and using multimeters and wattmeters, were processed and analyzed using Matlab.

3.2.2 Calibration

To ensure that the measurements of all channels were comparable to each other and as accurate to the actual values as possible the NI devices needed to be calibrated. This was done using the oscilloscope, with probes, and the LabView script described above. Figure 3.1 shows the connection of the NI devices, the power box and a 10 Ω potentiometer. The current/voltage converter was clamped around the conductor where I flows and the voltage probe was connected to measure U.

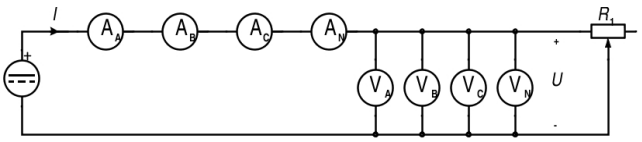

Figure 3.1: The setup used when calibrating the National Instruments devices.

Firstly the power box was replaced by a short circuit and a measurement for 0 V and 0 A was taken. Secondly the power box was connected and set to maximum voltage, 29.2 V, the potentiometer was tuned to achieve a current of 5.3 A and a second measurement was taken. Since the relation between voltage/current and the value provided by the devices is linear, two measurements was sufficient. Using the Matlab function `Polyfit` the coefficients for the linear

relations were obtained and inserted in scaling blocks, one for each channel, in the LabView script. The measurements were repeated to ensure that the desired effect was achieved.

3.3 Transformers

The transformers used in the laboratory experiments were the ones ordered and used by Christensson and Lingärde [25]. These, three single-phase transformers, one three-phase three-legged transformer and one three-phase five-legged transformer, see Figure 3.2 to 3.4, were made according to specifications which define the Geomagnetically Induced Current (GIC) immune transformer patented by AF Klercker Alaküla and Lindahl [1].

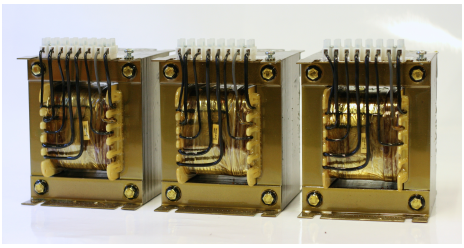

Specifications	
Power	800 VA
Frequency	50 – 60 Hz
Primary	0 – 127 – 220 V
Secondary	127 V / 5.2 A
Tertiary	0 – 42 – 73 V / 1.8 A

(a) Single-phase, hight = 15 cm

Figure 3.2: The single-phase transformers equipped with compensation windings for GIC immunity.

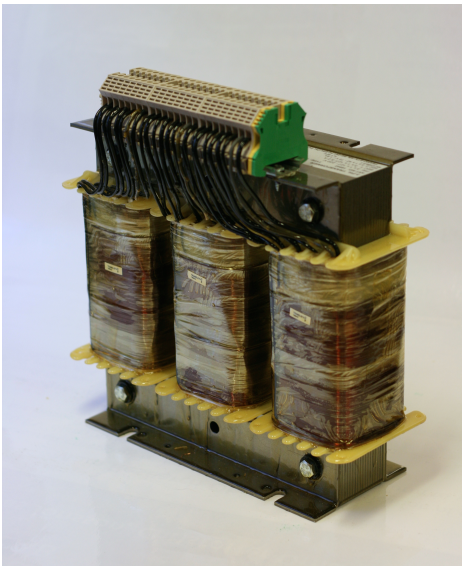

Specifications	
Power	2400 VA
Frequency	50 – 60 Hz
Primary	0 – 127 – 220 V
Secondary	127 V / 5.2 A
Tertiary	0 – 42 – 73 V / 1.8 A

(a) Three-phase three-legged, hight = 26 cm

Figure 3.3: The three-phase three-legged transformer equipped with compensation windings for GIC immunity.

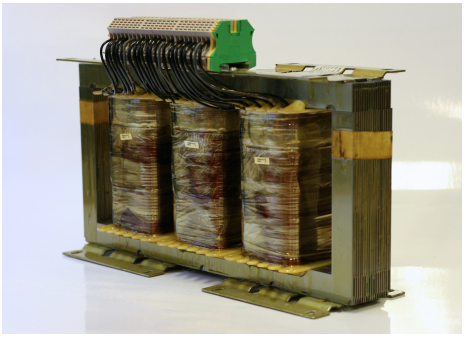

Specifications	
Power	2400 VA
Frequency	50 – 60 Hz
Primary	0 – 127 – 220 V
Secondary	127 V / 5.2 A
Tertiary	0 – 42 – 73 V / 1.8 A

(a) Three-phase five-legged, hight = 21.5 cm

Figure 3.4: The three-phase five-legged transformer equipped with compensation windings for GIC immunity.

3.3.1 Sequential Parameters

To ensure that all the sequential parameters were measured analogous the values found in [25] were discarded and measurements for all relevant, to this project, configurations were made according to Appendix B, see Table 3.2.

Fault Currents and Voltages

The sequential parameters in Table 3.2 indicate the difference in characteristics between the lab transformers and the typical full scale power transformer. The

Transformer type	Z_0 [Ω]	Z_1 [Ω]
Single $\mathrm{Dy_n}$	$0.6690 + 0.0854i$	$0.5604 + 0.0842i$
Single $\mathrm{Y_Ny_n}$	$0.7070 + 0.1202i$	$0.5877 + 0.1101i$
3-legged $\mathrm{Dy_n}$	$0.7284 + 0.1203i$	$0.6530 + 0.1099i$
3-legged $\mathrm{Y_Ny_n}$	$0.7669 + 0.1303i$	$0.6876 + 0.0861i$
5-legged $\mathrm{Dy_n}$	$0.7566 + 0.1032i$	$0.6508 + 0.1153i$
5-legged $\mathrm{Y_Ny_n}$	$0.8015 + 0.0996i$	$0.6904 + 0.0869i$

Table 3.2: Zero-, Z_0, and positive-sequence, Z_1, impedances for the different transformer configurations obtained from measurements described in Appendix B.

small scale transformers do not live up to the standards which apply to those in the MVA range and have high resistances in reference to their reactances. Due to this the X/R ratio has shifted, from approximately 10 to about $1/7$, causing the fault current (I_F) and maximum line-to-ground voltage during fault (U_{max}) levels to turn, compared to Figure 2.14 and 2.16, and their scaling to increase, see Figure 3.5 and 3.6 which show the results of running the calculations described in subsection 2.2.3 and 2.2.4 using the single-phase transformer sequence impedances in Table 3.2.

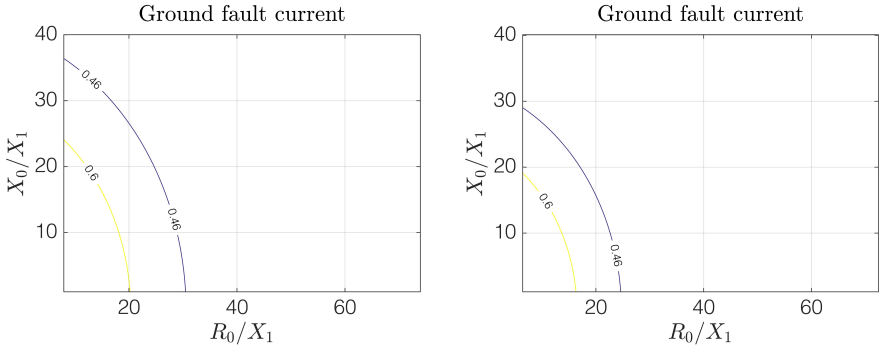

(a) $\mathrm{Dy_n}$-configuration (b) $\mathrm{Y_Ny_n}$-configuration

Figure 3.5: Analytical fault current to three-phase short-circuit current ratio levels for the single-phase lab transformer, Figure 3.2, acquired through analytical calculations as described in subsection 2.2.3.

Regarding the I_F and U_{max} curves, the dependencies of resistance and reactance have practically shifted. The resistive I_F curve is now lower than the reactive and the voltage dip formerly found in phase B, dotted, of a resistively grounded transformer can now be found in the C phase, dashed, of a reactively grounded transformer, see Figure 3.7 and 3.8 compared to Figure 2.15 and 2.17.

The delay in starting point in these graphs is due to the fact that $Z_{0trafo} \neq 0$ and thus the Z_0 is not zero when the coefficient used with positive-sequence reactance in Z_0 (n) is. Comparing the $\mathrm{Dy_n}$- and $\mathrm{Y_Ny_n}$-configuration shows no great differences and since the same is true for the different core types, and due

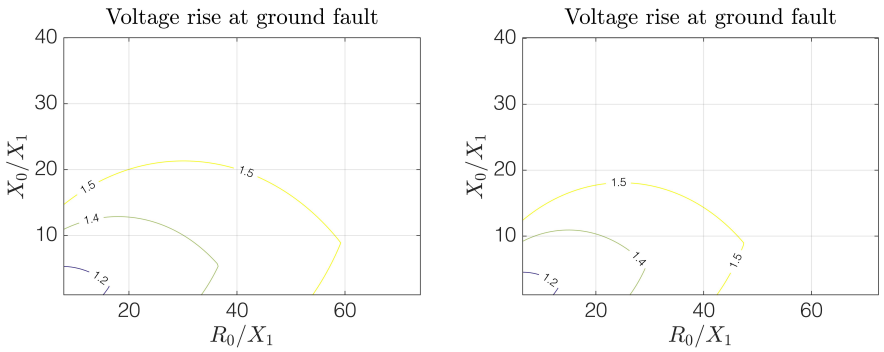

(a) $\mathrm{Dy_n}$-configuration (b) $\mathrm{Y_N y_n}$-configuration

Figure 3.6: Analytical voltage levels for the single-phase transformer, Figure 3.2 acquired through analytical calculations as described in subsection 2.2.4.

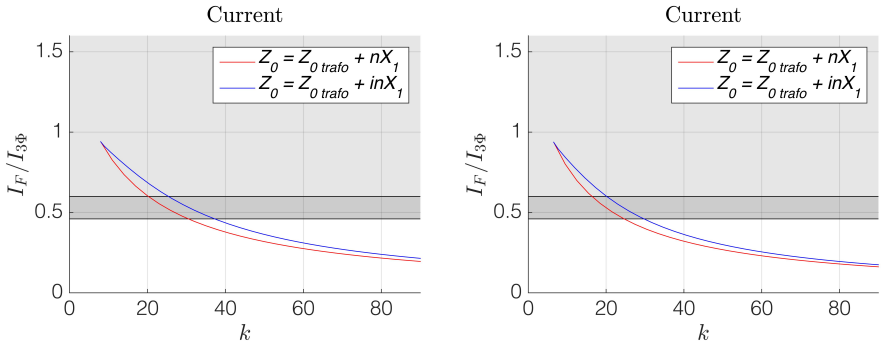

(a) $\mathrm{Dy_n}$-configuration (b) $\mathrm{Y_N y_n}$-configuration

Figure 3.7: Analytical fault current to three-phase short-circuit current ratio curves for the single-phase lab transformer, Figure 3.2, acquired through analytical calculations as described in subsection 2.2.3.

to the fact that these small scale transformers are not representative for the full scale versions in this respect, the corresponding graphs for the three-phase three-legged and five-legged are omitted.

Comparing the $\mathrm{Dy_n}$- and $\mathrm{Y_N y_n}$-configuration of the single-phase transformers shows no great differences. The starting points have approximately the same magnitude though it is at a slightly higher impedance ratio (k) in the $\mathrm{Dy_n}$-configuration.

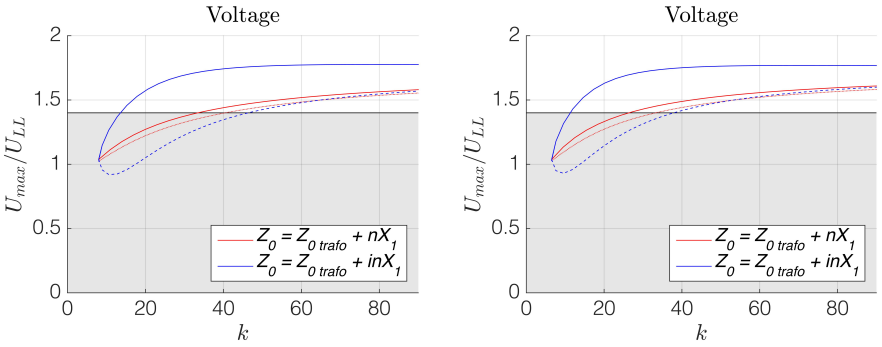

(a) $\mathrm{Dy_n}$-configuration (b) $\mathrm{Y_N y_n}$-configuration

Figure 3.8: Analytical line-to-ground voltage curves of the healthy phases, dashed and dotted, and their maximum, solid, for resistive, red, and reactive, blue, Z_0 during a bolted single-line-to-ground fault with the single-phase transformer, Figure 3.2 acquired through analytical calculations as described in subsection 2.2.4.

Fault Currents and Voltages with Compensation

Assuming that the compensation windings are perfect, they should completely cancel out the zero-sequence reactance (X_0). Considering this, setting $X_0 = 0$, and rerunning the calculations results in the graphs in Figure 3.9 to 3.12. For the same reason as for the un-compensated transformers, only the graphs of the single-phase transformers are shown here.

The fault current and voltage levels, see Figure 3.9 and 3.10, follow their uncompensated counterparts exactly though the removal of X_{0trafo} allows them to reach the ${}^{R_0}/_{X_1}$ axis. The changes in the fault current and voltage curves, see Figure 3.11 and 3.12, are hardly noticeable due to the low X_{0trafo} value in respect to the much larger R_{0trafo} value. Since $k = {}^{Z_0}/_{X_1}$ this small difference in Z_0 has no apparent effect, except that the rotation lowers the starting point voltage in phase B, see the dotted lines. If the ${}^{X_0}/_{R_0}$ ration had been that of a commercial power transformer, about 10 instead of ${}^1/_7$, the impact would have been the starting point moving closer to the theoretical starting point, $k = 0$, ${}^{I_F}/_{I_{3\Phi}} = 1.5$. Precisely how far depends on the ratio.

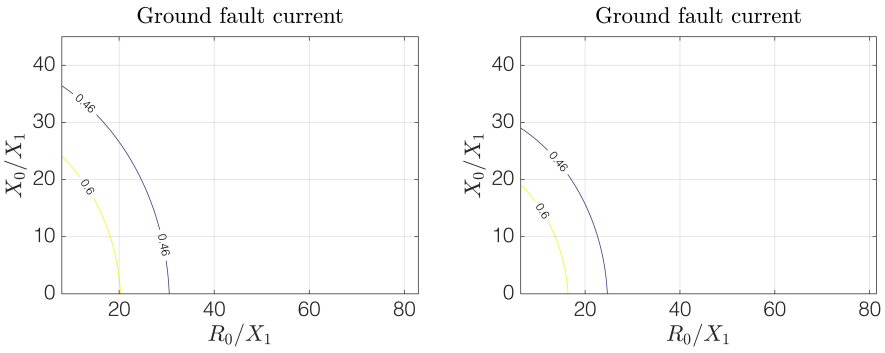

(a) $\mathrm{Dy_n}$-configuration (b) $\mathrm{Y_N y_n}$-configuration

Figure 3.9: Analytical fault current to three-phase short-circuit current ratio levels for the compensated single-phase lab transformer, Figure 3.2, acquired through analytical calculations as described in subsection 2.2.3.

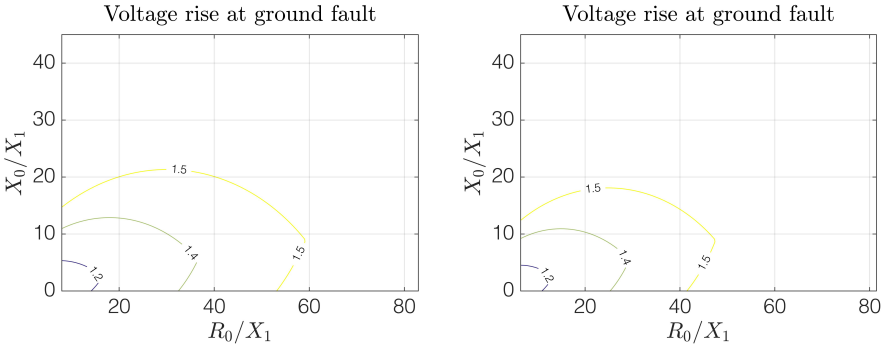

(a) $\mathrm{Dy_n}$-configuration (b) $\mathrm{Y_N y_n}$-configuration

Figure 3.10: Analytical voltage levels for the compensated single-phase transformer, Figure 3.2 acquired through analytical calculations as described in subsection 2.2.4.

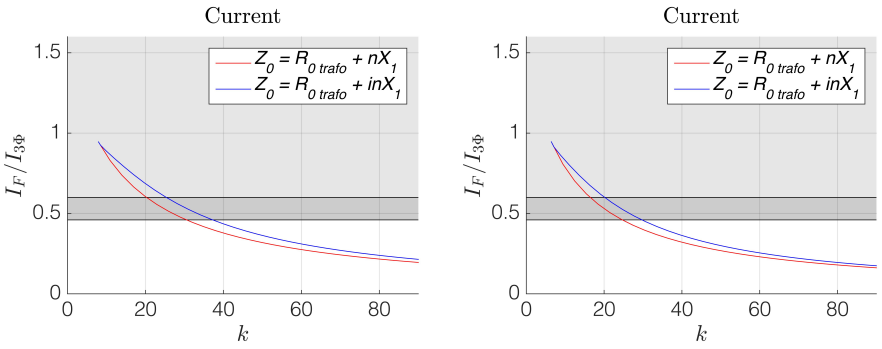

(a) $\mathrm{Dy_n}$-configuration (b) $\mathrm{Y_N y_n}$-configuration

Figure 3.11: Analytical fault current to three-phase short-circuit current ratio curves for the compensated single-phase lab transformer, Figure 3.2, acquired through analytical calculations as described in subsection 2.2.3.

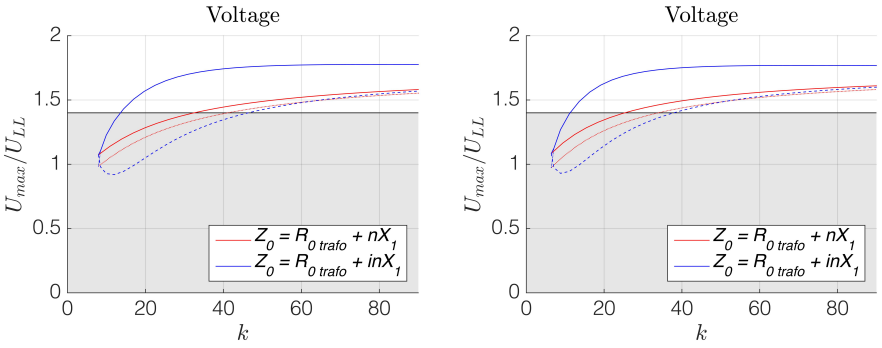

(a) $\mathrm{Dy_n}$-configuration (b) $\mathrm{Y_N y_n}$-configuration

Figure 3.12: Analytical line-to-ground voltage curves of the healthy phases, dashed and dotted, and their maximum, solid, for resistive, red, and reactive, blue, Z_0 during a bolted single-line-to-ground fault with the compensated single-phase transformer, Figure 3.2 acquired through analytical calculations as described in subsection 2.2.4.

For the experiments the assumption, $X_0 = 0$, is not valid and therefore the compensation impedances (Z_{comp}), see Table 3.3, were determined as described in Appendix B.

Transformer	Z_{comp} [Ω]
Single $\mathrm{Dy_n}$	$0.8113 + 0.0701i$
Single $\mathrm{Y_N y_n}$	$0.8104 + 0.0390i$
3-legged $\mathrm{Dy_n}$	$0.9723 + 0.1200i$
3-legged $\mathrm{Y_N y_n}$	$0.9533 + 0.0863i$
5-legged $\mathrm{Dy_n}$	$0.9656 + 0.1250i$
5-legged $\mathrm{Y_N y_n}$	$0.9516 + 0.0947i$

Table 3.3: Impedance in the compensation windings obtained from measurements described in Appendix B.

3.3.2 Model Parameters and Saturation

To facilitate the running of simulations of the experiment, or other tests involving these transformers, standard tests, [26], were executed and magnetization curves rendered. The resulting parameters are listed in Table 3.4 and 3.5. A description of the methods used in this specific case can be found in Appendix B.

	Single-phase [p.u.]	3-legged [p.u.]	5-legged [p.u.]
R_{DCP220}	4.473×10^{-2}	4.770×10^{-2}	4.786×10^{-2}
R_{DCP127}	1.422×10^{-2}	1.754×10^{-2}	1.745×10^{-2}
R_{DCS127}	1.622×10^{-2}	2.029×10^{-2}	2.024×10^{-2}
R_{DCT73}	0.2252	0.2735	0.2792
R_{DCT42}	0.1318	0.1680	0.1472
R_{wP220}	1.409×10^{-2}	-4.721×10^{-3}	-4.655×10^{-3}
R_{wP127}	7.878×10^{-3}	8.624×10^{-3}	8.608×10^{-3}
R_{wS127}	8.934×10^{-3}	9.564×10^{-3}	9.451×10^{-3}
R_{wT73}	0.1064	0.1414	0.1409
R_{wT42}	5.453×10^{-2}	7.828×10^{-2}	7.768×10^{-2}
R_m	49.47	40.38	33.12
L_{lP220}	1.155×10^{-5}	2.024×10^{-7}	-6.328×10^{-7}
L_{lP127}	9.274×10^{-6}	7.739×10^{-6}	8.011×10^{-6}
L_{lS127}	3.441×10^{-6}	3.596×10^{-6}	3.515×10^{-6}
L_{lT73}	6.620×10^{-5}	9.132×10^{-5}	9.508×10^{-5}
L_{lT42}	4.316×10^{-5}	6.357×10^{-5}	6.314×10^{-5}
L_m	5.421×10^{-2}	6.779×10^{-2}	2.951×10^{-2}

Table 3.4: Transformer parameters, in p.u. obtained from measurements described in Appendix B.

Transformer	Coordinates [p.u.]
Single Dy_n	[0 0 ; 0.0671 2.0557 ; 0.45404 2.7324]
Single $Y_N y_n$	[0 0 ; 0.1127 1.1757 ; 0.65539 1.5551]
3-legged Dy_n	[0 0 ; 0.0931 0.72268 ; 0.72577 0.88015]
3-legged $Y_N y_n$	[0 0 ; 0.2771 0.43536 ; 1.1226 0.50055]
5-legged Dy_n	[0 0 ; 0.2304 0.73252 ; 0.83319 0.87281]
5-legged $Y_N y_n$	[0 0 ; 0.4232 0.42864 ; 1.3979 0.49882]

Table 3.5: Saturation characteristics, in p.u., for the transformer configurations.

3.4 Summary

The results of this project should be reproducible with equipment which match the specifications in this chapter. It should also be possible to get similar results through simulations using the parameters listed in subsection 3.3.2.

As Table 3.2 and 3.3 shows, these small scale lab transformers have high resistances in reference to their low reactances. The reactance to resistance ratios, X/R, are about $1/7 - 1/10$ whereas the corresponding value for a full scale power transformer is approximately 10. This causes the single-line-to-ground fault current and voltage grounding dependencies to shift.

Chapter 4

Experiments

In order to repeat the experiment it is vital to have a good understanding of how it was executed. This chapter describes the methods used in the different tests and also provides schematics for the corresponding circuits. In each of the three parts, Fault Currents and Voltages, GIC Effects and Full System Test, both the regular and the compensated transformer setups are covered.

4.1 Ground Faults on Transformer

4.1.1 Regular Transformer

The analytical calculations of the fault currents and voltages, see section 3.3.1, do not account for a number of circumstances that the actual transformer might be subject to and due to this measurements are of interest. Each transformer type was connected according to Figure 4.1 and 4.2 in turn. During all the tests the fault impedance (Z_F) was kept at zero, that is all tests are of bolted faults, while the neutral point impedance (Z_N) was varied by connecting different combinations of the smoothing impedances or potentiometers. Each measurement was started with the circuit breaker, S_1, open and ended with it closed, to provide scaling information since the tests could not be performed at rated voltage. Instead the voltage was set to a level which resulted in a fault current (I_F) between 5.0 and 5.2 A. Since all measurements were instantaneous values they needed to be converted to complex or root-mean-square (rms) values and this was achieved through Discrete Fourier Transform (DFT), see Appendix C. The start voltage is the line-to-ground voltage (U_{LG}) which was used as a base for the voltage rise. The line-to-neutral voltage (U_{LN}) was also determined from the start measurements, (4.1), and in turn used to calculate the three-phase short-circuit current ($I_{3\Phi}$), (4.2). The measurements taken with S_1 closed provide the maximum line-to-ground voltage during fault (U_{max}), (4.3), I_F, the zero-sequence impedance (Z_0), (4.4), and the impedance ratio k, (4.5).

$$\overline{U_{LN}} = \overline{U_{LG}} - \overline{U_{NG}} \tag{4.1}$$

$$\overline{I_{3\Phi}} = \frac{\overline{U_{LN}}}{\overline{Z_1}} \tag{4.2}$$

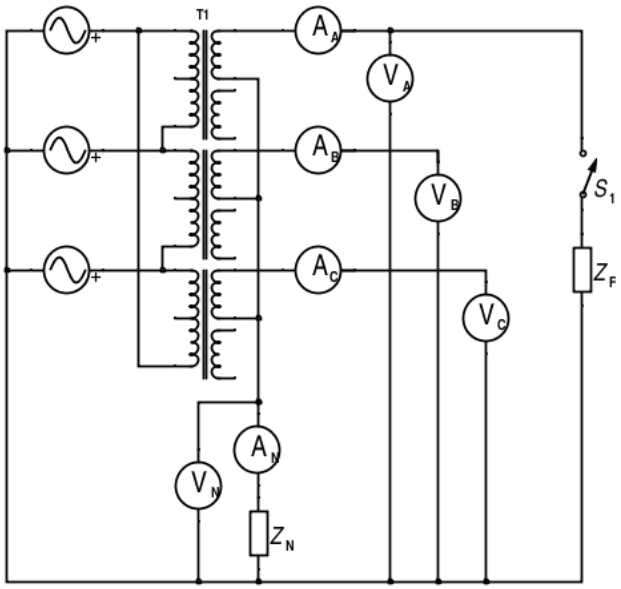

Figure 4.1: Schematic for the $\mathrm{Dy_n}$-connected fault on transformer measurement circuit.

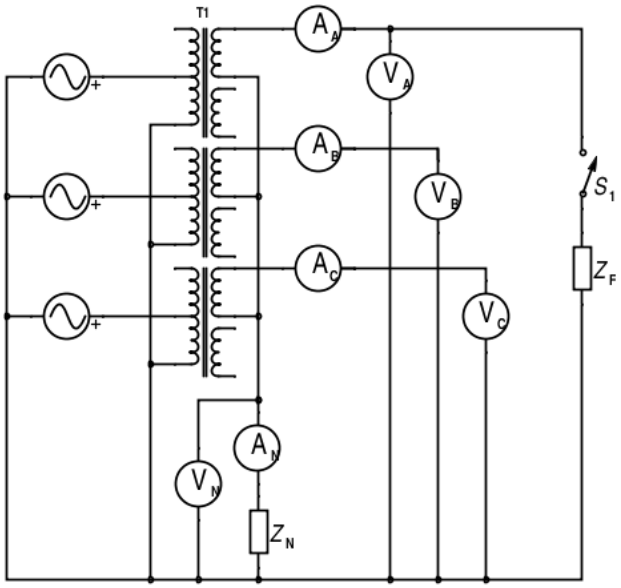

Figure 4.2: Schematic for the $\mathrm{Y_N y_n}$-connected fault on transformer measurement circuit.

$$U_{max} = \max\left(\left|\overline{U_{BG}}\right|, \left|\overline{U_{CG}}\right|\right) \tag{4.3}$$

$$\overline{Z_N} = \Re\left(\frac{\overline{U_{N_F}}}{\overline{I_{N_F}}}\right) + i\Im\left(\frac{\overline{U_{N_F}}}{\overline{I_{N_F}}}\right) \tag{4.4}$$

$$k = \left|\frac{\overline{Z_0}}{X_1}\right| = \left|\frac{\overline{Z_{0trafo}} + 3\overline{Z_N}}{X_1}\right| \tag{4.5}$$

4.1.2 GIC Immune Transformer

In theory the compensation impedance (Z_{comp}) of the Geomagnetically Induced Current (GIC) immune transformer should cancel out the zero-sequence reactance (X_0) exactly, see section 3.3.1. To determine the impact of this winding it was added to the setup according to Figure 4.3 or 4.4 depending on the configuration and testing was performed like for the regular transformer. In this case the impedance ratio (k) was calculated in two different ways, (4.5) and (4.6), to account for the Z_{comp} resistance.

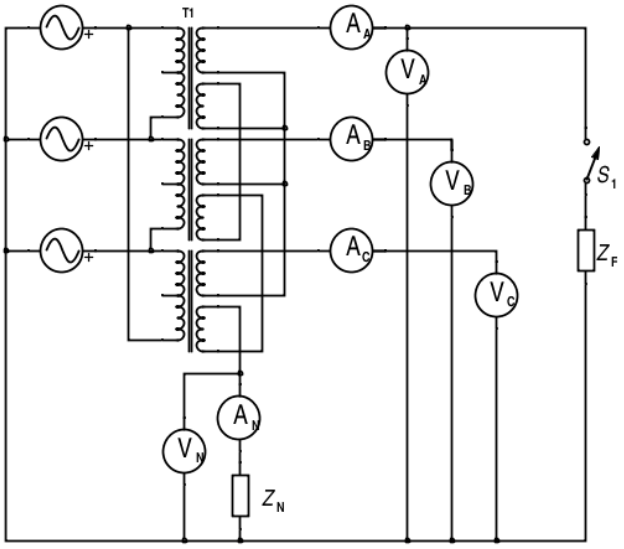

Figure 4.3: Schematic for the compensated Dy_n-connected fault on transformer measurement circuit.

$$k = \left|\frac{\overline{Z_0}}{X_1}\right| = \left|\frac{\overline{Z_{0trafo}} - \Im(\overline{Z_{comp}}) + 3(\overline{Z_N} + \Re(\overline{Z_{comp}}))}{X_1}\right| \tag{4.6}$$

$$\overline{Z_{0trafo}} - \Im(\overline{Z_{comp}}) \approx R_{0trafo}$$

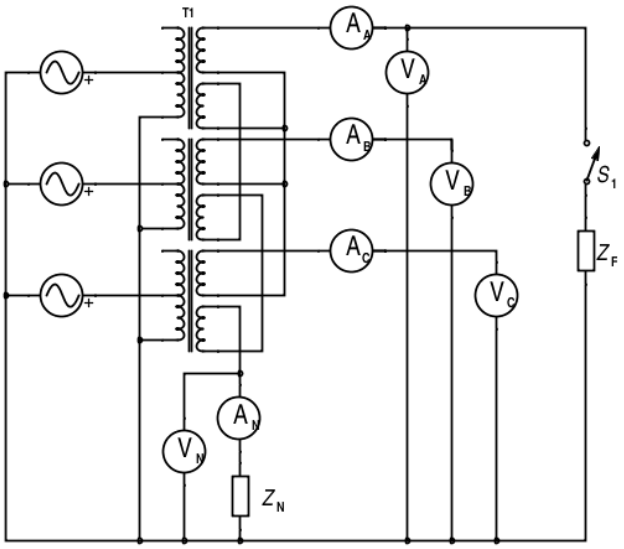

Figure 4.4: Schematic for the compensated $Y_N y_n$-connected fault on transformer measurement circuit.

4.2 GIC in System Model

4.2.1 Regular Transformer

The effects of GICs have been investigated and reported a number of times, e.g. [2–5, 12, 14, 15]. It is however of importance to determine how the lab transformers operate during similar conditions. Since GICs have very low frequencies it is sufficient to model them with a Direct Current (DC) source. Due to the low DC resistance of the lab setup, the relatively high DC currents needed and the uncertainty of the power box's operation under these circumstances the car battery in series with a potentiometer was connected in parallel 0.5 Ω, two parallel 1 Ω potentiometers, to achieve a stable DC current supply without adding too much DC resistance. The potentiometer in series with the battery was used to control the DC current magnitude and to do this the remaining potentiometers were needed since the larger ones could not sustain the high DC current required in order to obtain some of the wanted DC currents through the transformer, see Table 4.1. Figure 4.5 and 4.6 show the schematics used. Preferably all measurements would be taken simultaneously but since there were a limited number of National Instruments (NI) devices the experiment was performed twice for each configuration, one when measuring on the primary side and one on the secondary side, to obtain all the relevant data.

The primary side measurements were used when calculating the reactive power loss (Q), see (4.7), in each phase due to GIC and the secondary side measurements provided the information from which the harmonic content was derived, using DFT.

Experimental [A]	Of nominal current [%]	Representing [A]
0.11	2.115	10
0.22	4.231	20
0.55	10.58	50
1.09	20.96	100
1.64	31.54	150
2.18	41.92	200
2.73	52.50	250
3.27	62.29	300
3.49	67.12	320

Table 4.1: DC current levels used to model the GIC during the GIC in system model experiment.

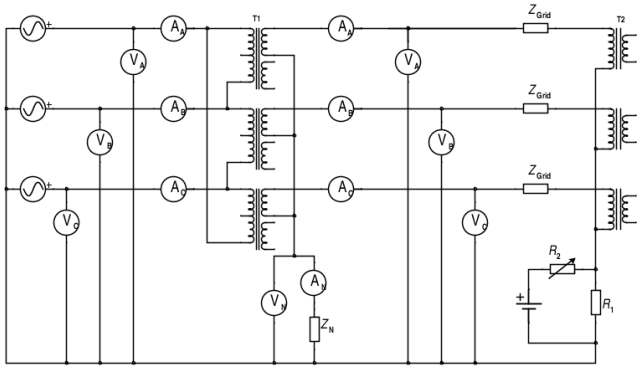

Figure 4.5: Schematic for the Dy_n-connected GIC in system model measurement circuit.

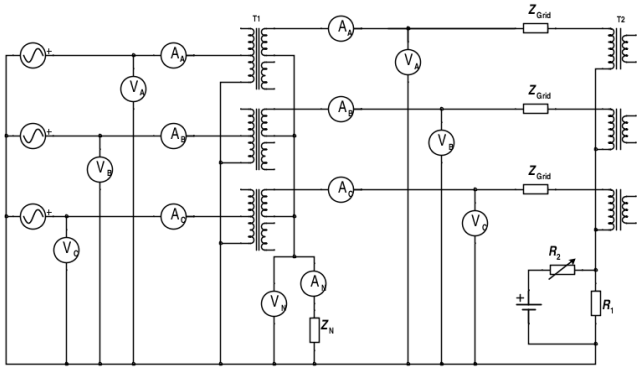

Figure 4.6: Schematic for the Y_NY_n-connected GIC in system model measurement circuit.

$$Q_i = \Im\left(\frac{\overline{U_i}}{\sqrt{2}} \times \frac{\overline{I_i}^*}{\sqrt{2}}\right) \tag{4.7}$$

In one case, the three-phase five-legged transformer, measurements were also taken with load applied to transformer T_2, see Figure 4.7 and 4.8, to assure that this does not affect the effects of GIC.

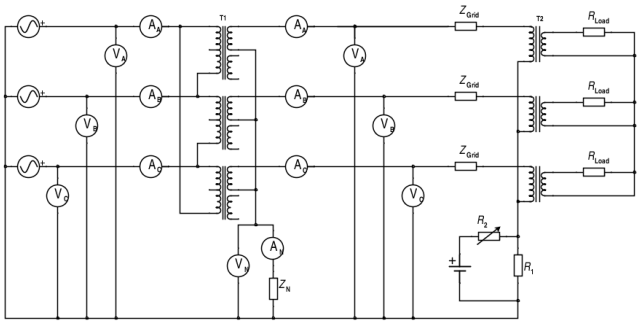

Figure 4.7: Schematic for the $\mathrm{Dy_n}$-connected GIC in system model measurement circuit with load.

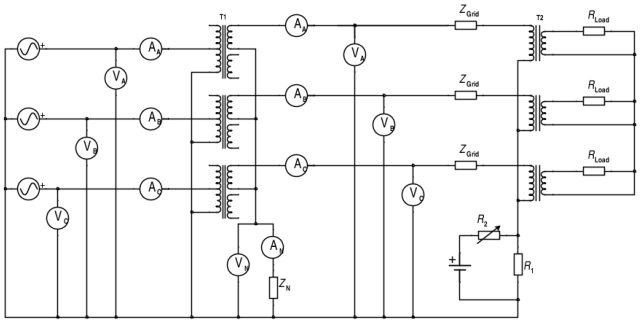

Figure 4.8: Schematic for the $\mathrm{Y_N y_n}$-connected GIC in system model measurement circuit with load.

4.2.2 GIC Immune Transformer

The compensation windings are meant to negate the effects the zero-sequence-like GICs. How well this is achieved by the lab transformers is essential information and therefore, measurements were taken for the GIC levels in Table 4.1 in the setups shown in Figure 4.9 and 4.10.

As in the regular transformer case, the experiment was repeated twice to obtain measurements on both the primary, Q, and secondary, harmonics, side. No tests were made at load in this instance.

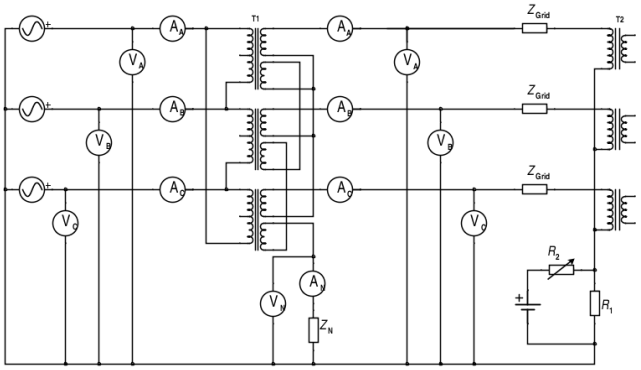

Figure 4.9: Schematic for the compensated Dy_n-connected GIC in system model measurement circuit.

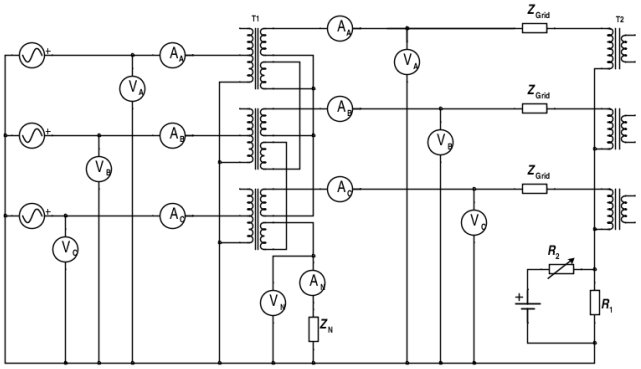

Figure 4.10: Schematic for the compensated Y_Ny_n-connected GIC in system model measurement circuit.

4.3 Ground Faults in System Model

4.3.1 Regular Transformer

A transformer is rarely connected solely on the primary side, but usually part of a larger grid. Due to this it is relevant to investigate how a single-line-to-ground fault would appear in these conditions. To achieve this the equipment was set up according to Figure 4.11 and 4.12 and measurements were taken for the same reactance combinations and resistances as in section 4.1.

The data was processed in the same way as in section 4.1.

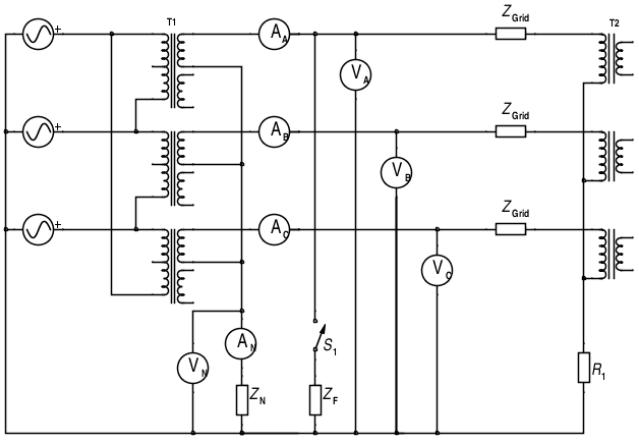

Figure 4.11: Schematic for the $\mathrm{Dy_n}$-connected fault in system model measurement circuit.

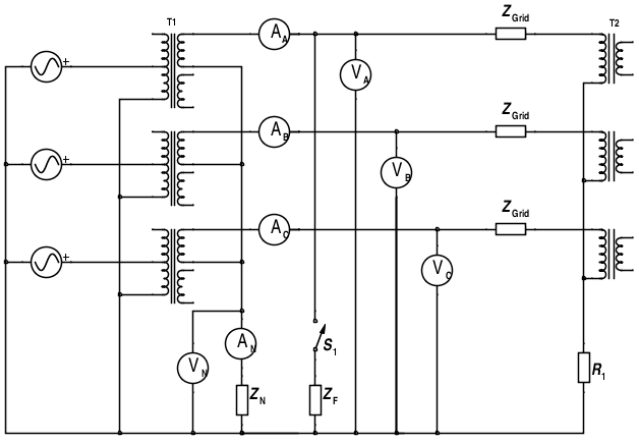

Figure 4.12: Schematic for the $\mathrm{Y_N y_n}$-connected fault in system model measurement circuit.

4.3.2 GIC Immune Transformer

One goal of this project was to determine the need of Z_N when using GIC immune transformers. To achieve this measurements on the transformer, when connected in a manner similar to a grid, utilizing the compensation windings were required. The setups in Figure 4.13 and 4.14 were implemented, measurements taken and processed as in the case of the regular transformer. As in subsection 4.1.2 k was determined both according to (4.5) and (4.6).

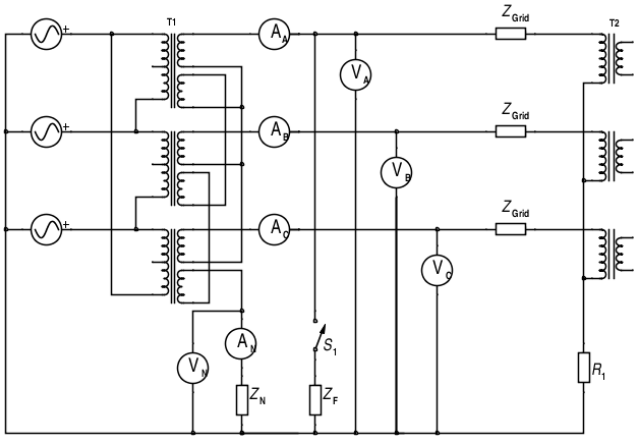

Figure 4.13: Schematic for the compensated $\mathrm{Dy_n}$-connected fault in system model measurement circuit.

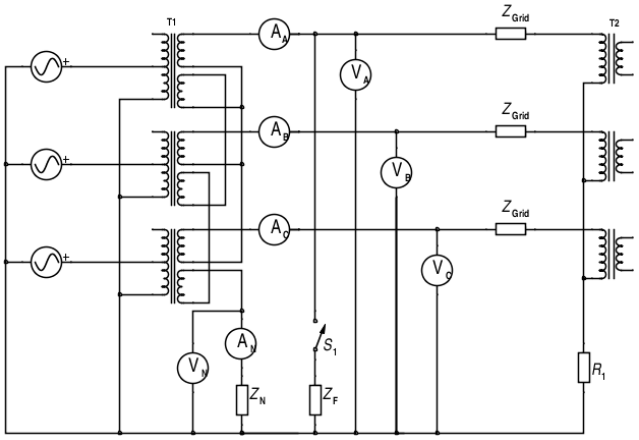

Figure 4.14: Schematic for the compensated $\mathrm{Y_N y_n}$-connected fault in system model measurement circuit.

4.4 Summary

Utilizing the schematics shown in this chapter and performing the computations on the obtained measurements, one should obtain approximately the same results as during this experiment which will be presented in chapter 5.

Chapter 5

Experiment Results

This chapter contains the experiment results. It begins with the ground fault on transformer graphs, followed by the outcome of the Geomagnetically Induced Current (GIC) and ground faults in system model tests, all obtained as described in chapter 4. Each property, fault current and voltage for the fault cases and second harmonic and reactive power in the GIC case, is evaluated, for the regular transformers after which a comparison with the GIC immune version is performed.

5.1 Ground Faults on Transformer

5.1.1 Regular Transformer

Since the analytical calculations preformed in section 3.3 depict faults on only transformers, without grid connection, measurements on an equivalent setup are of interest. Since the low reactance to resistance ratio, $X/R \approx 1/7$ instead of approximately 10, of the lab transformers renders them un-representative of the full scale transformers in this respect and the differences between transformer types are minor, only the results of the single-phase transformers are shown in this section. Figure 5.1 shows the fault current (I_F) to three-phase short-circuit current ($I_{3\Phi}$) ratios obtained through computations of the measurements, as described in section 4.1.

In comparison with the analytical graph in Figure 3.7, these measured fault current begin at lower values than the analytical and are not as smooth.

When the maximum line-to-ground voltage during fault is concerned Figure 5.2 shows the measurements taken during the experiment in section 4.1.

Naturally the measured curves are not as smooth as the analytical ones, they also have a lesser incline and thus exceed the voltage limit, dashed line, at higher k-values than their analytical counterparts.

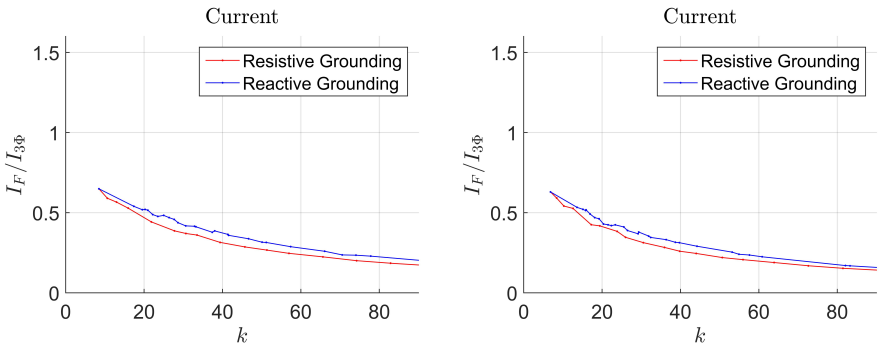

(a) $\mathrm{Dy_n}$-configuration (b) $\mathrm{Y_N y_n}$-configuration

Figure 5.1: Single-line-to-ground fault on transformer current for the single-phase transformers. k is the impedance ratio, Z_0/X_1.

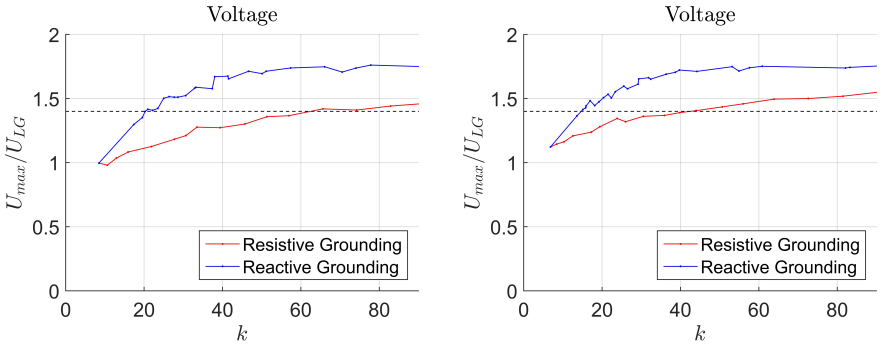

(a) $\mathrm{Dy_n}$-configuration (b) $\mathrm{Y_N y_n}$-configuration

Figure 5.2: Maximum phase voltage during single-line-to-ground fault on transformer for the single-phase transformers. k is the impedance ratio, Z_0/X_1.

5.1.2 GIC Immune Transformer

To make the comparison between the regular and the GIC immune transformers easier the graphs which utilized the same expression for k, see (4.5), are shown here, Figure 5.3 and 5.4. As a result of this the levels in the two versions at a specific k refer to their respective response to the same neutral point impedance (Z_N). In general the fault currents in the GIC immune transformers are lower than those in the corresponding regular transformer. Due to the apparent similarity between core types and the lab transformers not being representative to the full scale transformers in this respect, this section does not show the results of the three-phase transformers.

The sound line-to-ground voltage rises in the GIC immune transformers have higher starting values than their regular counterparts and they are closer together. As a result of this the resistive curves exceed the limit, dashed line, at

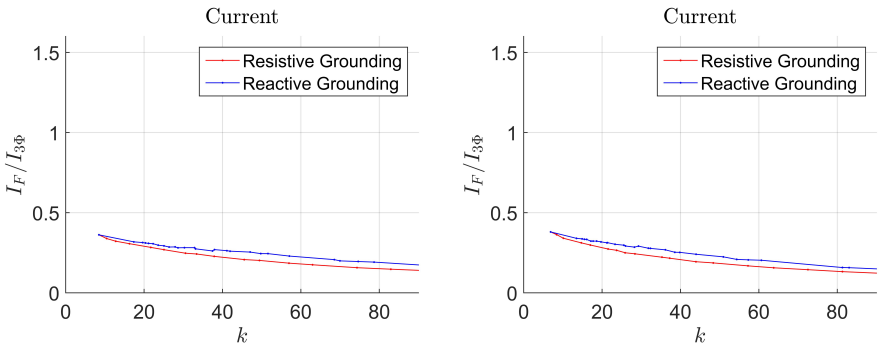

(a) $\mathrm{Dy_n}$-configuration (b) $\mathrm{Y_N y_n}$-configuration

Figure 5.3: Single-line-to-ground fault on transformer current for the compensated single-phase transformers. k is the impedance ratio, Z_0/X_1.

a lower k-value in this configuration while the reactive do so at approximately the same value.

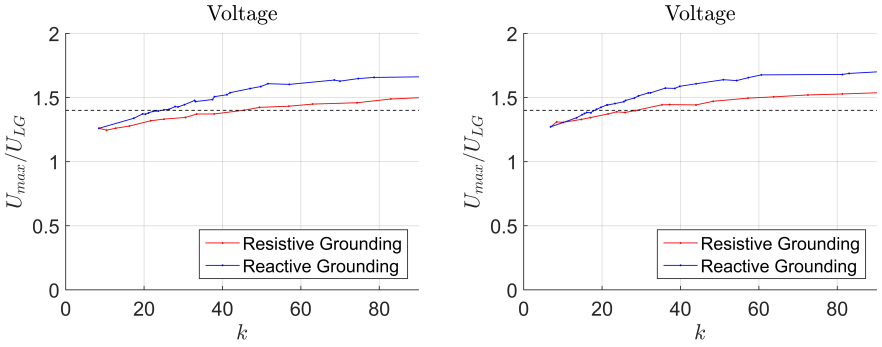

(a) $\mathrm{Dy_n}$-configuration (b) $\mathrm{Y_N y_n}$-configuration

Figure 5.4: Maximum phase voltage during single-line-to-ground fault on transformer for the single-phase transformers. k is the impedance ratio, Z_0/X_1.

In comparison with the analytical graphs these are less curved and though they have higher starting points they exceed the limit at higher k values than their counterparts.

Adding the compensation winding to the setup does not have as great an impact on the fault currents and maximum line-to-ground voltages during fault as expected. This is due to the abnormal zero-sequence reactance (X_0) to zero-sequence resistance (R_0) ratio as negating the reactance hardly alters the zero-sequence impedance (Z_0) at all whereas it with a normal ratio would become more or less zero.

5.2 GIC in System Model

5.2.1 Regular Transformer

The second harmonics due to the artificial GIC, derived as described in section 4.2, are shown in Figure 5.5 to Figure 5.7. In these the relationship between GICs and this harmonic is apparent. When comparing the Dy_n- and Y_Ny_n-configuration in Figure 5.5 the levels are slightly higher in the Y_Ny_n-connected phases.

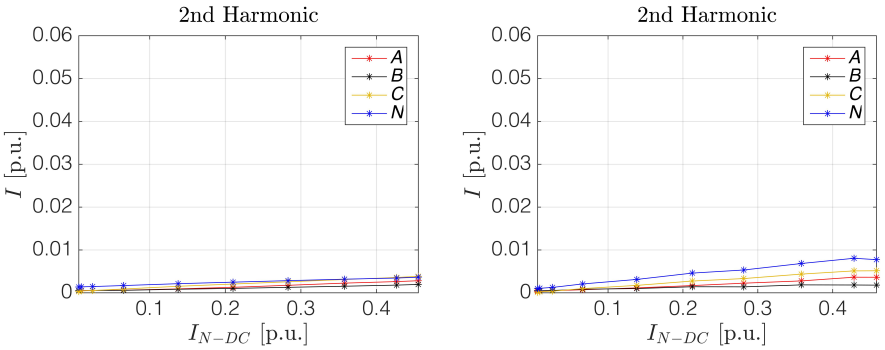

(a) Dy_n-configuration (b) Y_Ny_n-configuration

Figure 5.5: Second harmonic currents due to GIC in the regular single-phase transformers.

In the three-phase three-legged transformer there is no notable difference between the two configurations, see Figure 5.6.

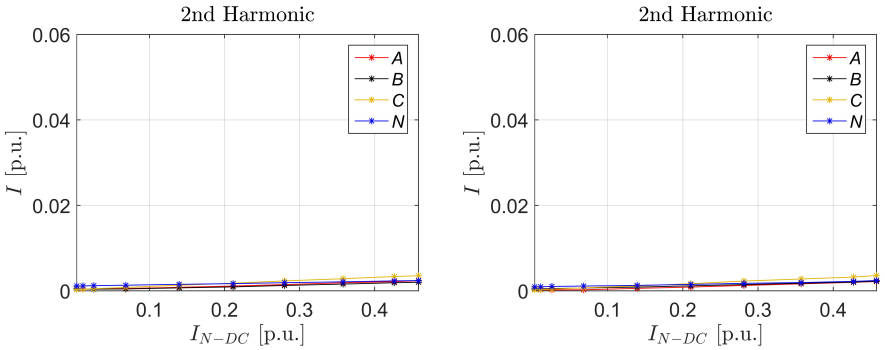

(a) Dy_n-configuration (b) Y_Ny_n-configuration

Figure 5.6: Second harmonic currents due to GIC in the regular three-phase three-legged transformer.

As in the single-phase case, the three-phase five-legged transformer is more sensitive in the Y_Ny_n-configuration than in the Dy_n, see Figure 5.7. In a comparison between the core types, all in Y_Ny_n-configuration, the five-legged trans-

former has the highest dependence while the three-legged has the lowest, this is also true for the $\mathrm{Dy_n}$-configurations though the differences are not as large.

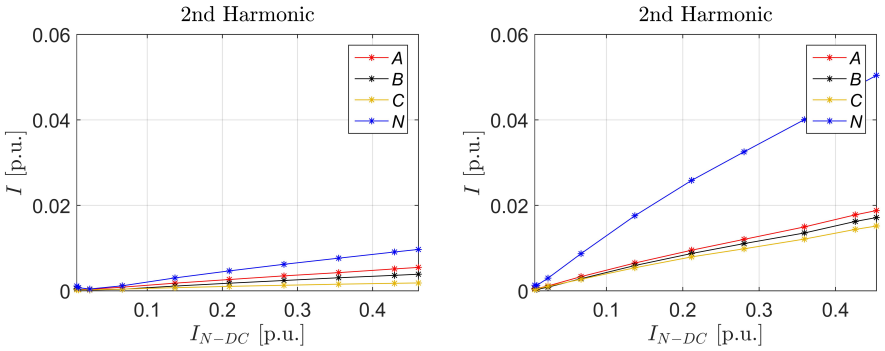

(a) $\mathrm{Dy_n}$-configuration (b) $\mathrm{Y_N y_n}$-configuration

Figure 5.7: Second harmonic currents due to GIC in the regular three-phase five-legged transformer.

Though the graphs of the three-phase five-legged transformer with load, Figure 5.8 are not as linear as the ones without load, they still have approximately the same magnitude.

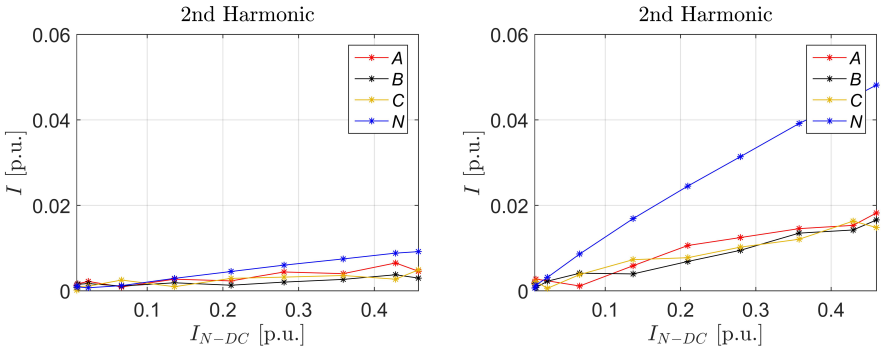

(a) $\mathrm{Dy_n}$-configuration (b) $\mathrm{Y_N y_n}$-configuration

Figure 5.8: Second harmonic currents due to GIC in the regular three-phase five-legged transformer at load.

The reactive power (Q) losses in the single-phase transformers are connected to the GIC in the system, see Figure 5.9. As the graphs show, these losses do not depend on the configuration used but increase with the magnitude of the GIC.

Figure 5.10 illustrates that though the impact of configuration is insignificant, the impact of core type is not. In the three-phase three-legged transformer the GICs do not affect the reactive losses notably.

In the case of the three-phase five-legged transformer the reactive losses are,

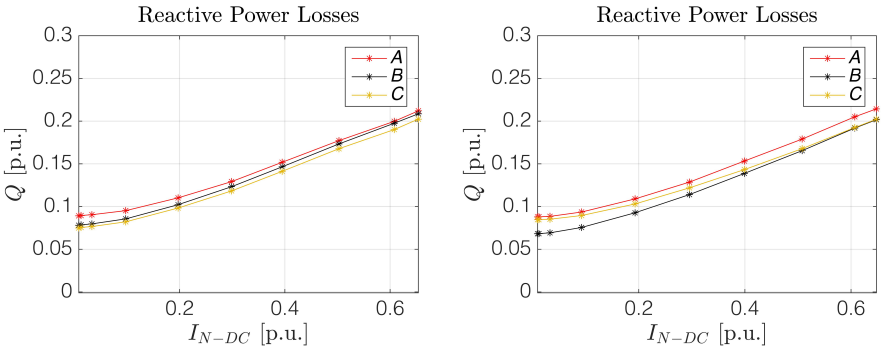

(a) $\mathrm{Dy_n}$-configuration (b) $\mathrm{Y_N y_n}$-configuration

Figure 5.9: reactive power (Q) due to Geomagnetically Induced Current (GIC) in the regular single-phase transformers.

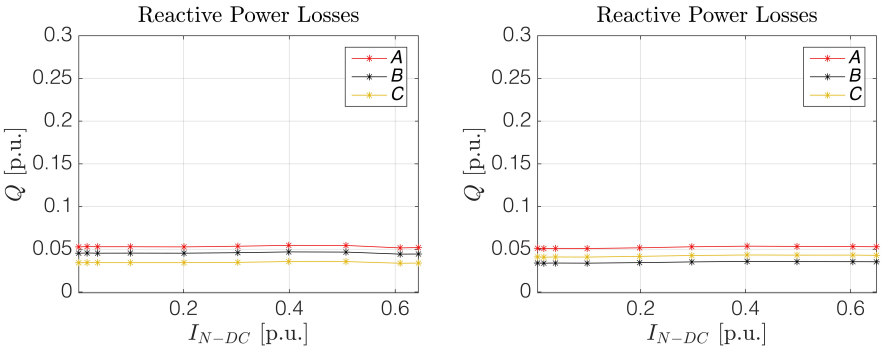

(a) $\mathrm{Dy_n}$-configuration (b) $\mathrm{Y_N y_n}$-configuration

Figure 5.10: reactive power (Q) due to Geomagnetically Induced Current (GIC) in the regular three-phase three-legged transformer.

once again, dependent of the GIC. Comparing the core types with each other, in regard to Q losses, the three-legged transformer is affected the least by GICs and the single-phase transformer the most.

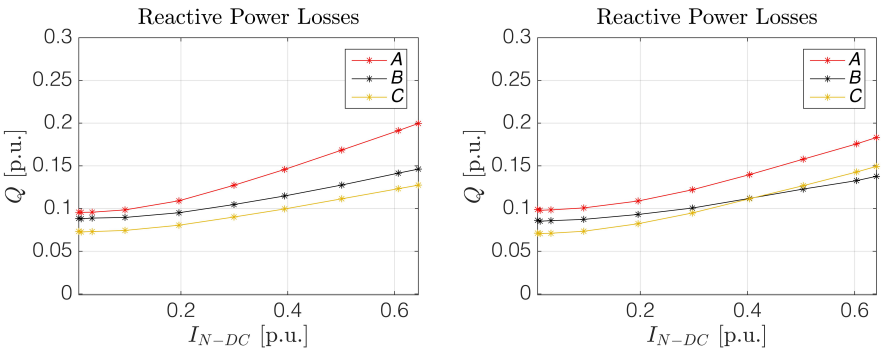

(a) Dy_n-configuration (b) $Y_N y_n$-configuration

Figure 5.11: reactive power (Q) due to Geomagnetically Induced Current (GIC) in the regular three-phase five-legged transformer.

5.2.2 GIC Immune Transformer

Introducing the compensation winding to the setup results in the GIC immune transformer. The consequences of GIC in this version of the transformers is shown in Figure 5.12 to 5.17. The magnitude of second harmonics in the single-phase transformers does not depend on the connection type, that is the Dy_n- and $Y_N y_n$-configuration produce equivalent graphs, see Figure 5.12. In comparison to the regular transformers the intensity of the harmonic has decreased to approximately $^2/_3$ for the Dy_n- and $^1/_2$ for the $Y_N y_n$-configuration.

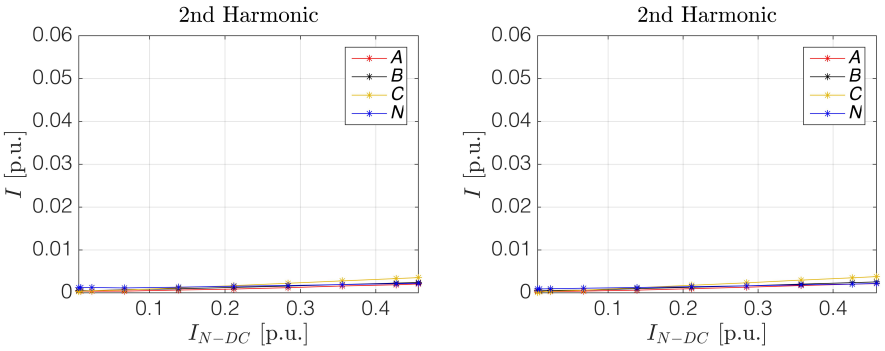

(a) Dy_n-configuration (b) $Y_N y_n$-configuration

Figure 5.12: Second harmonic currents due to GIC in the compensated single-phase transformers.

The graphs for the three-phase three-legged transformer hardly display any differences, see Figure 5.13, neither between the configurations nor in reference to the regular version.

Figure 5.14 shows the second harmonic magnitudes due to GIC in the five-legged GIC immune transformer. As for the other two core types the configura-

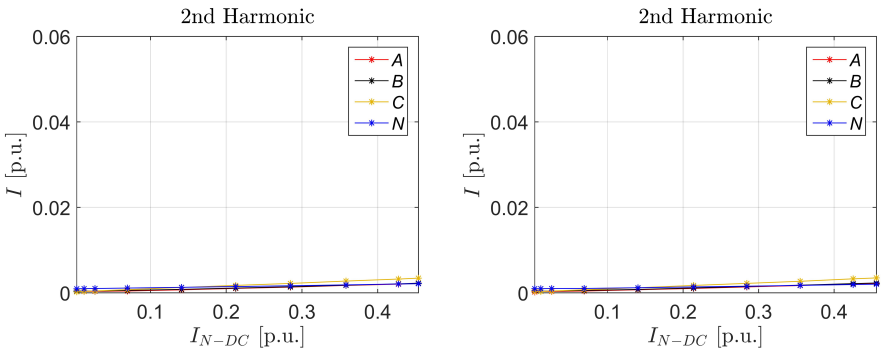

(a) Dy_n-configuration (b) Y_Ny_n-configuration

Figure 5.13: Second harmonic currents due to GIC in the compensated three-phase three-legged transformer.

tion is of no importance. In comparison to the regular transformer the harmonic intensity has been reduced to approximately $1/2$ and $1/10$ in the Dy_n- and Y_Ny_n-configuration respectively. The magnitude of the harmonic is roughly the same in all the compensated cases.

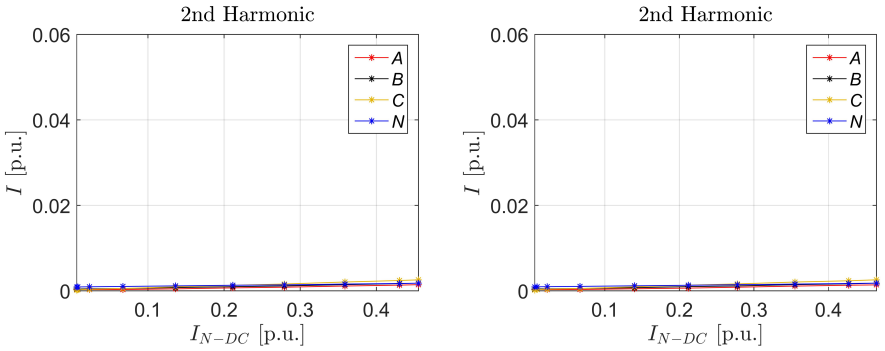

(a) Dy_n-configuration (b) Y_Ny_n-configuration

Figure 5.14: Second harmonic currents due to GIC in the compensated three-phase five-legged transformer.

Considering the Q loss graphs in Figure 5.15 to 5.17 it becomes apparent that neither the configuration nor the core type is of any significance when it comes to the these losses in a GIC immune transformer. All cases result in Q losses which have no correlation with the artificial GIC induced in the system. Comparing this with the regular transformers the losses start at the same level but while the single-phase and the five-legged transformer experience an increase in losses as the GIC increases in the regular version it is kept constant in the immune.

Since there was no dependence in the three-legged transformer to begin with

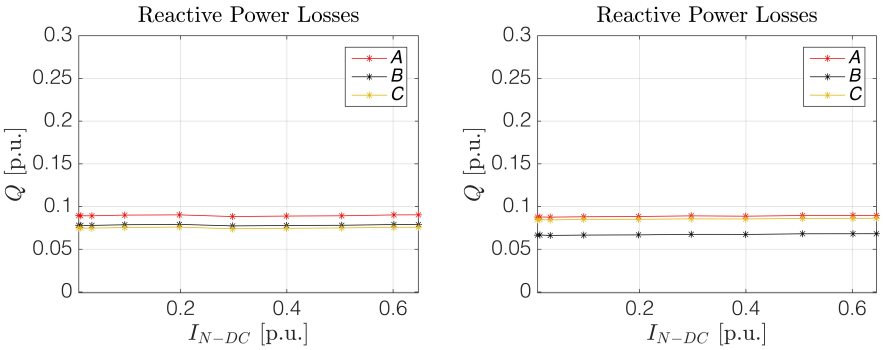

(a) Dy_n-configuration (b) $Y_N y_n$-configuration

Figure 5.15: reactive power (Q) due to Geomagnetically Induced Current (GIC) in the compensated single-phase transformers.

there are no effects due to the introduction of the compensation winding in this type.

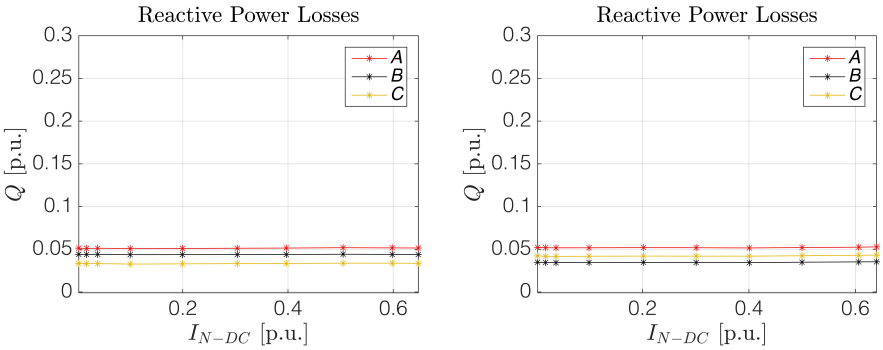

(a) Dy_n-configuration (b) $Y_N y_n$-configuration

Figure 5.16: reactive power (Q) due to Geomagnetically Induced Current (GIC) in the compensated three-phase three-legged transformer.

Though the effects of GICs are completely eliminated by adding the compensation winding it has the most effect in the single-phase transformers, since they were the most sensitive to GICs, in respect to Q losses, whereas it is of no importance in the three-legged transformer.

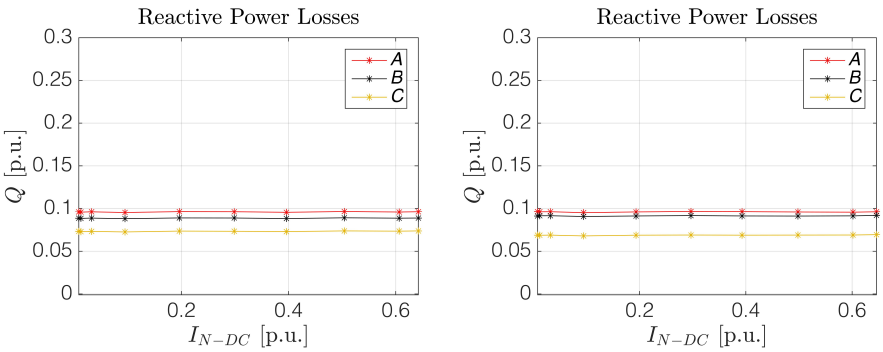

(a) Dy_n-configuration (b) Y_Ny_n-configuration

Figure 5.17: reactive power (Q) due to Geomagnetically Induced Current (GIC) in the compensated three-phase five-legged transformer.

5.3 Ground Faults in System Model

5.3.1 Regular Transformer

As in section 5.1 only the single-phase transformer transformer results are shown due to the similarities between core types and the fact that the lab transformers characteristics render them un-representative of the full scale transformers. In comparison to the measurements made on only the transformers, see Figure 5.1, the fault currents have a slower decrease when connected the grid model which cause them to have higher magnitudes at a certain k, see Figure 5.18.

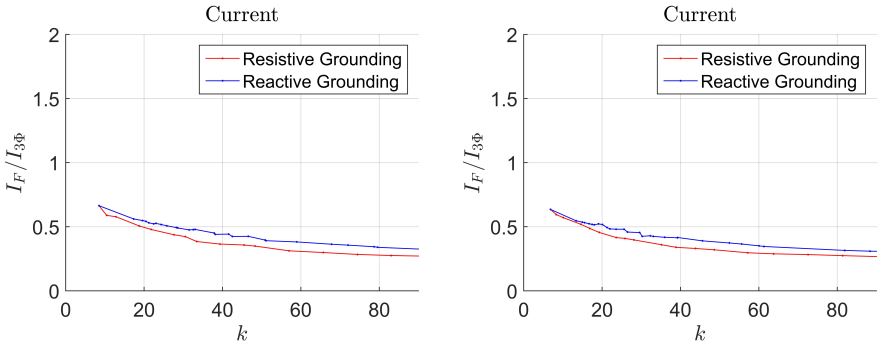

(a) Dy_n-configuration (b) Y_Ny_n-configuration

Figure 5.18: Single-line-to-ground fault in system model current for the single-phase transformers. k in the impedance ratio, Z_0/X_1.

In comparison with the measurements taken on the transformers separately, Figure 5.2, these have lesser voltage inclines and higher Z_Ns can be used before exceeding the limit, Figure 5.19.

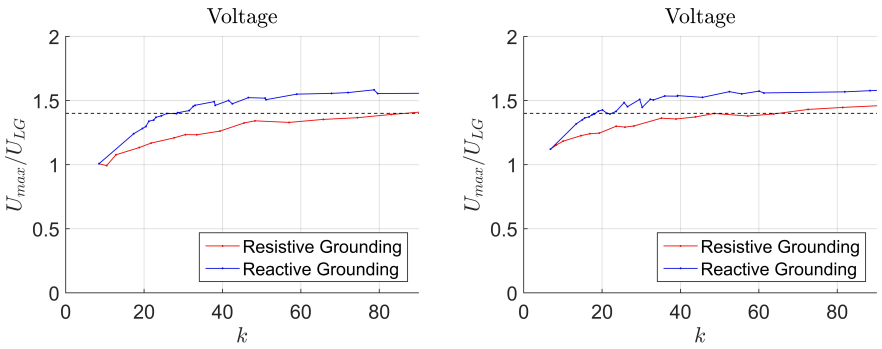

(a) Dy_n-configuration (b) Y_Ny_n-configuration

Figure 5.19: Maximum phase voltage during single-line-to-ground fault in system model for the single-phase transformers. k in the impedance ratio, Z_0/X_1.

5.3.2 GIC Immune Transformer

As for the regular transformers these fault currents, see Figure 5.20, decrease slower and thus have higher magnitudes at a specified k than those of the transformers which were not connected to a grid, Figure 5.3.

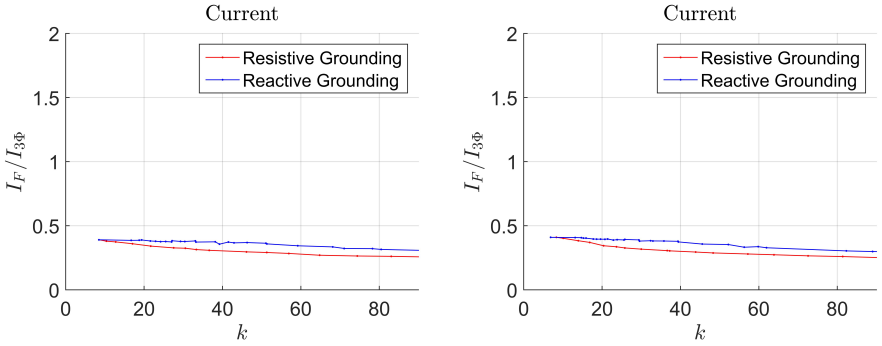

(a) Dy_n-configuration (b) Y_Ny_n-configuration

Figure 5.20: Single-line-to-ground fault in system model current for the compensated single-phase transformers. k in the impedance ratio, Z_0/X_1.

Comparing these fault currents with the ones of the regular transformers these starting points are lower and the graphs are straighter causing them to exit the figure at approximately the same levels. The magnitudes achieved with a low Z_N here requires a significantly higher value in the regular counterparts.

In comparison with the transformers without grid, Figure 5.4, the maximum line-to-ground voltage during fault starting points are approximately the same, the incline is lower and the difference between resistive and reactive grounding is smaller, see Figure 5.21.

Adding the compensation winding to the grid attached transformers signifi-

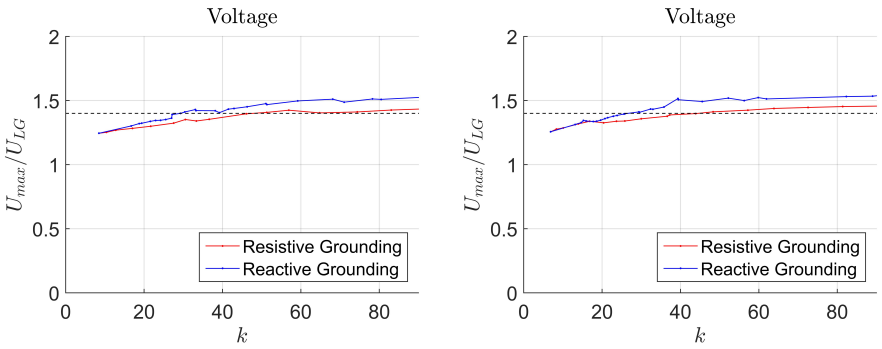

(a) $\mathrm{Dy_n}$-configuration (b) $\mathrm{Y_N y_n}$-configuration

Figure 5.21: Maximum phase voltage during single-line-to-ground fault in system model for the compensated single-phase transformers. k in the impedance ratio, Z_0/X_1.

cantly increases the maximum line-to-ground voltage during fault (U_{max}) magnitudes at the starting points, it also decreases the incline and the difference between resistive and reactive grounding. Despite this the compensated transformers require lower k-values to prevent the maximum line-to-ground voltage during fault from rising beyond the specified limit. These conclusions are, however, not valid for the full scale system due to the lab transformers X/R ratio differing too much from the typical full scale value.

5.4 Summary

The measuring results presented in this chapter show that though there are some differences, the analytical calculations are quite similar to the actual behavior of both the regular and the GIC immune transformers. The beneficial effects of adding the compensation windings, in regard to the reduction of half-cycle saturation and the associated second harmonic content and reactive power losses have been established. The tests have also confirmed the significance of core type and delta windings which were mentioned in chapter 2.

In addition to this the full system experiment indicates that connecting a grid leads to higher fault currents, lower maximum line-to-ground voltages during fault and a decrease in their incline. Due to the abnormal X_0 to R_0 ratio of the lab transformers these measurements can not be used to draw any conclusions when it comes to the Z_N required for obtaining the same maximum line-to-ground voltage during fault and fault current with the GIC immune transformer as with the regular version. Because of this simulations are needed to determine the effects of adding the compensation windings to the transformer setup. The simulation method and the results are presented in chapter 6 and 7 respectively.

Chapter 6

Simulations

The SimPowerSystem model and the parameters involved in the simulations of the a full scale version of the experiment setup are presented in this chapter.

6.1 SimPowerSystem Model

The simulations were performed using four SimPowerSystem models, Dy_n- and Y_Ny_n-configured, with and without compensation winding. Figure 6.1 shows the un-compensated Y_Ny_n-configured model. Each single-phase transformer block measured the currents and voltages in its three windings and the neutral point impedance (Z_N) block measured the neutral point correspondents. These measurements were collected and saved to the Matlab work space by the multimeter and scope blocks respectively.

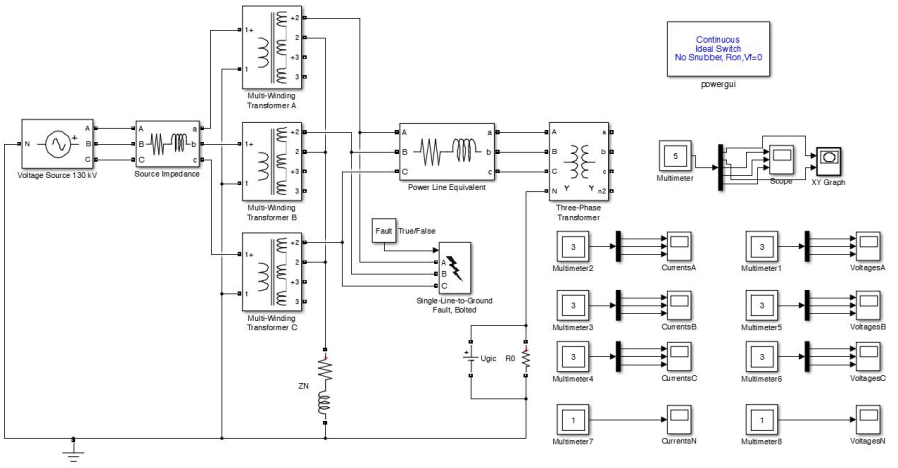

Figure 6.1: The Simulink model of the Y_Ny_n-configured setup without compensation.

The voltage source block was set to generate a 50 Hz, 130 kV voltage with a phase of 0.75°, which was the default value. Since the voltage source block is

ideal, i.e. it has no losses, an impedance block was added to model the source impedance which was given a resistance of 0.01 Ω and a inductance of 0.0637 H.

The single-phase transformers were set to be saturable and given the values in Table 6.1. While the power, frequency and voltages in this table were purpose defined, corresponding to the Finnish power grid, the resistances, impedances and saturation characteristic were the default values.

Parameter	Dy_n-value	$Y_N y_n$-value
Nominal Power [MVA]	$400/3$	$400/3$
Frequency [Hz]	50	50
Winding 1 Nominal rms Voltage [kV]	130	$130/\sqrt{3}$
Winding 2 Nominal rms Voltage [kV]	$400/\sqrt{3}$	$400/\sqrt{3}$
Winding 3 Nominal rms Voltage [kV]	$400/(3\sqrt{3})$	$400/(3\sqrt{3})$
Winding Resistance [p.u.]	0.005	0.005
Winding Leakage Inductance [p.u.]	0.02	0.02
Magnetization Resistance [p.u.]	50	50
Saturation Characteristic [p.u.] Point 1	0, 0	0, 0
Point 2	0.0024, 1.2	0.0024, 1.2
Point 3	1.0, 1.52	1.0, 1.52

Table 6.1: Parameters used in the single-phase transformer blocks.

The Z_N block consists of a resistive and an inductive part. To simplify the varying of these during the simulations they were set to R_N and L_N respectively. Since having a zero impedance in this block is not permitted a very small resistance, 10^{-12} Ω, was added in the block. This was also the resistance assigned in the fault block, since the same restriction applies here. This block was set to simulate a fault between phase A and ground when the external constant $Fault$ is 1, which was controlled from a script.

The impedance block to the right of the single-phase transformers represents the power line losses and was given the resistance 10 Ω and inductance 0.5 H which corresponds to approximately 300 km of 400 kV power lines.

As in the lab experiments a three-phase transformer was used to acquire a neutral point. The parameters in this block were chosen to match the ones in the single-phase transformers though the default value for the secondary winding was used since it was not connected. Contrary to the single-phase transformers this one was not set to be saturable.

The Direct Current (DC) voltage source U_{GIC} was used to achieve the difference in potential which results in a Geomagnetically Induced Current (GIC). The magnitude of this voltage was set from the script. Since this, just as the voltage source, is an ideal component there was no need to connect it in parallel with a resistance.

The power gui block specified that the simulations ran continuously and that the switching devices used were ideal, their snubbers were disabled and their on resistance (R_{ON}) and forward voltage (U_f) were zero. Other settings used were the use of the `ode23bt` solver and a stop time defined as T_{stop}, set from the script.

6.2 Method

The per unit (p.u.) bases used during the simulations are listed in Table 6.2.

Base	Value
S_{base}	400 MVA
U_{base1}	130 kV
U_{base2}	400 kV
I_{base1}	3077 A
I_{base2}	1000 A
Z_{base}	400 Ω

Table 6.2: The per unit (p.u.) bases used for the simulations.

6.2.1 GIC in System Model

To verify that the behaviors and effects found during the experiments on lab transformers applied to the SimPowerSystem models, simulations were performed on the un-compensated model, with Z_N set to zero and to the Finnish value, $\overline{Z_N} = 2.5 + 120i\ \Omega$, as well as on the compensated model. In these tests the *Fault* variable was kept zero, no fault, and the GIC voltage, U_{GIC}, was increased from 0 to 3.75×10^{-3} p.u., i.e. 0 to 1.5 kV, in steps corresponding to 300 V. Since the values obtained from the scope blocks did not have a fixed sampling time they were converted to that in the experiment using the `interp1` function. These values were then processed as in section 4.2 to get the second harmonic and the reactive power losses (Q).

Since the GIC at a certain U_{GIC} level was not equal in the setups, due to the difference in resistance, both the harmonics and power losses were plotted as a function of U_{GIC} instead. For comparison the neutral point GIC current, $I_{N_{GIC}}$, was placed on top of the graphs.

6.2.2 Ground Faults in System Model

The relatively large resistances in the lab transformers made the experimental test results invalid and called for further examination. The SimPowerSystem models were utilized for this purpose. For scaling reasons it was vital to know the zero-sequence impedance (Z_0) and positive-sequence impedance (Z_1) values and since the numbers obtained from analytical calculations did not correspond to with actual simulation values the sequence impedances were determined through simulations and are thus the values as seen from the fault location.

A reference voltage was obtained through a short run on the un-compensated transformer model without fault. The fault block was then set to a three-phase short-circuit and the resulting three-phase short-circuit current ($I_{3\Phi}$) was acquired and converted to a complex value through the method described above. From this Z_1 was calculated as in (B.3). The Z_0 value was obtained by setting the fault to a single-line-to-ground fault, finding the fault current (I_F) and performingthe computation in (6.1), derived from (2.3), the results are shown in Table 6.3.

$$\overline{Z_0} = 3 \times \frac{\overline{U_A}}{\overline{I_F}} - 2 \times \overline{Z_1} \tag{6.1}$$

Configuration	Z_0 [Ω]	Z_1 [Ω]
$\mathrm{Dy_n}$	$3.9717 + 15.933i$	$7.6569 + 203.03i$
$\mathrm{Y_N y_n}$	$7.8984 + 202.85i$	$7.9347 + 202.84i$

Table 6.3: Zero-, Z_0, and positive-sequence, Z_1, impedances, as seen from the fault location, using the different transformer configurations.

Once the sequence impedances were established, the actual testing could be performed. Though these tests were all executed at nominal voltage, simulations without fault were still carried out to ensure that no initial voltage drops occurred over Z_N or the compensation winding and affected the results. A single-line-to-ground fault was then introduced and, as in the GIC case, the values from the scopes were converted to have fixed sampling time after which calculations were performed as for the experiment in section 4.1. This was implemented on the Finnish configuration and on the regular and GIC immune transformers, both while varying Z_N. In the regular case the neutral point reactance to neutral point resistance ratio was that of the Finnish Z_N, ${}^{X_N}/_{R_N} = 48$, while the corresponding value for the GIC immune setup was 200. The results from the two transformer types were finally plotted in separate figures with the Finnish point marked.

6.3 Summary

Performing simulations on models equivalent to the ones described here, using the same parameters, would produce the same results as presented in the next chapter.

Chapter 7

Simulation Results

The results of the simulations described in chapter 6 are presented here. First the Geomagnetically Induced Current (GIC) effects, in second harmonic and reactive power loss Q, are evaluated after which the fault behavior is analyzed.

7.1 GIC in System Model

The regular transformer shows a clear connection between the GIC voltage, U_{GIC}, neutral GIC current, I_{N-GIC}, and the second harmonic, see Figure 7.1. These graphs show no clear differences between the two connection types.

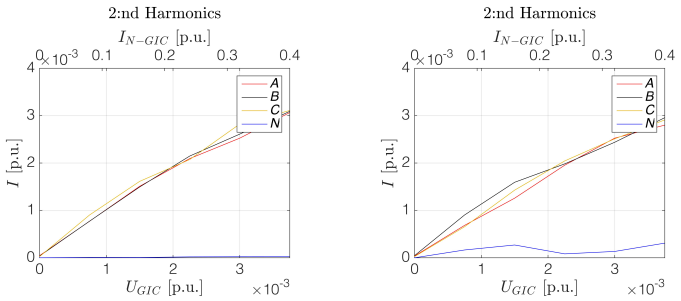

(a) $\mathrm{Dy_n}$-configuration (b) $\mathrm{Y_N y_n}$-configuration

Figure 7.1: Second harmonic currents due to GIC in a solidly grounded system.

Adding the Finnish neutral point impedance (Z_N) visibly lowers the harmonic magnitude and observing the I_{N-GIC} scale shows that the GIC current is lowered as well, see Figure 7.2. As in the solidly grounded setup, there are no apparent differences between the configurations.

Figure 7.3 shows the second harmonics in the GIC immune transformer. The effect of connecting the compensation winding is the complete removal of all harmonics, which is similar to the effects seen in the experiment. The GIC current has been slightly lowered as well, though not as much as with the Finnish grounding.

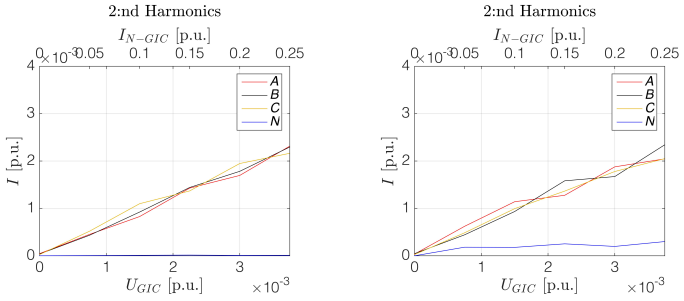

(a) $\mathrm{Dy_n}$-configuration (b) $\mathrm{Y_N y_n}$-configuration

Figure 7.2: Second harmonic currents due to GIC in a system with Finnish grounding, $Z_N = 2.5 + 120i\ \Omega$.

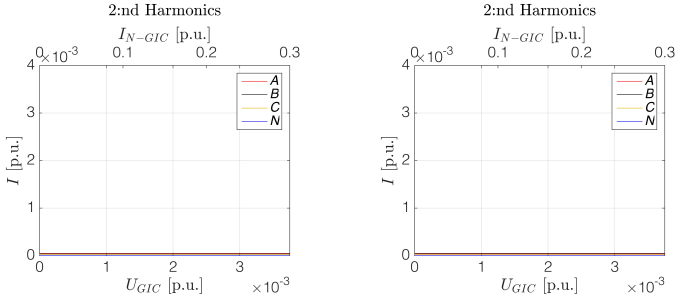

(a) $\mathrm{Dy_n}$-configuration (b) $\mathrm{Y_N y_n}$-configuration

Figure 7.3: Second harmonic currents due to GIC in a solidly grounded system with the GIC immune transformer.

It is not only the harmonic magnitude that is connected with U_{GIC}, the Q displays a similar dependency, see Figure 7.4. The results of the two configurations are practically identical.

As with the harmonics, adding the Finnish Z_N lowers both I_{N-GIC} and the Q magnitude, Figure 7.5. There are no apparent differences due to configuration visible here either.

The Q levels are kept at the initial values when using the GIC immune transformer, Figure 7.6, just as in the experiment. When GIC effects are considered the simulations show no dependence of connection type.

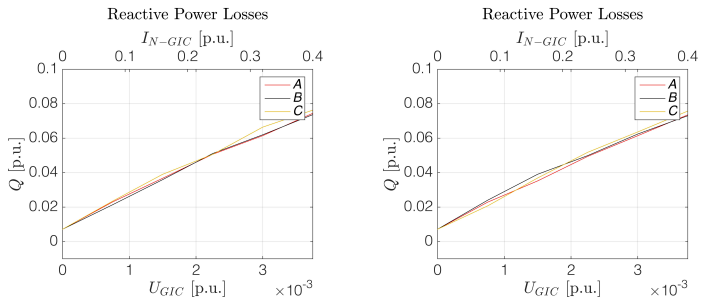

(a) $\mathrm{Dy_n}$-configuration (b) $\mathrm{Y_N y_n}$-configuration

Figure 7.4: reactive power (Q) losses due to GIC in a solidly grounded system.

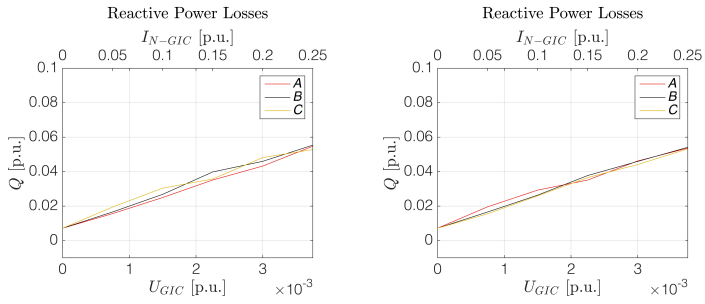

(a) $\mathrm{Dy_n}$-configuration (b) $\mathrm{Y_N y_n}$-configuration

Figure 7.5: reactive power (Q) losses due to GIC in a system with Finnish grounding, $Z_N = 2.5 + 120i\ \Omega$.

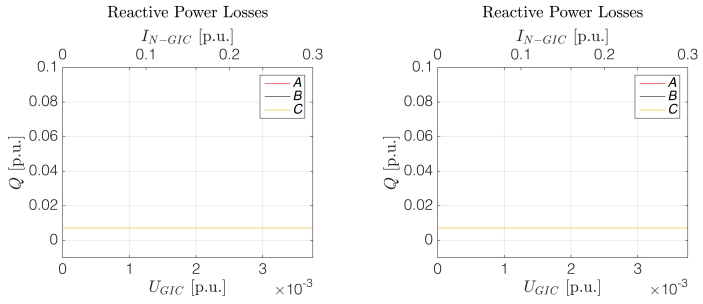

(a) $\mathrm{Dy_n}$-configuration (b) $\mathrm{Y_N y_n}$-configuration

Figure 7.6: reactive power (Q) losses due to GIC in a solidly grounded system with the GIC immune transformer.

7.2 Ground Faults in System Model

Regarding the fault current to three-phase short-circuit current ratio, $^{I_F}/_{I_{3\Phi}}$, curves in Figure 7.7 the most apparent difference is that the $\mathrm{Dy_n}$-configuration starts at a much lower impedance ratio (k), zero-sequence impedance to positive-sequence reactance, $k = Z_0/X_1$, than the $\mathrm{Y_N y_n}$-configuration which starts at $k \approx 1$. This is due to their Z_0 not being equal, which is also the cause to the horizontal distance of the Finnish point, marked by the red cross (×). The lesser impedance in the $\mathrm{Dy_n}$-configuration allows for a higher fault current to flow at a single-line-to-ground fault.

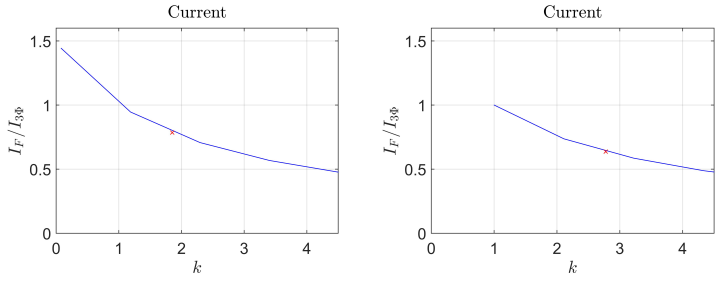

(a) $\mathrm{Dy_n}$-configuration (b) $\mathrm{Y_N y_n}$-configuration

Figure 7.7: Fault current in a regular transformer, the red cross (×) marks the Finnish point, $Z_N = 2.5 + 120i\ \Omega$.

Adding the compensation winding negates the zero-sequence reactance (X_0) established for the setup, see Figure 7.8. For the reason given above, this has a greater effect in the $\mathrm{Y_N y_n}$-configured transformer than in the $\mathrm{Dy_n}$. In this configuration the difference is hardly noticeable while the curve crosses the Finnish fault current level, marked by the dotted red line, at a significantly higher k with $\mathrm{Y_N y_n}$-connection.

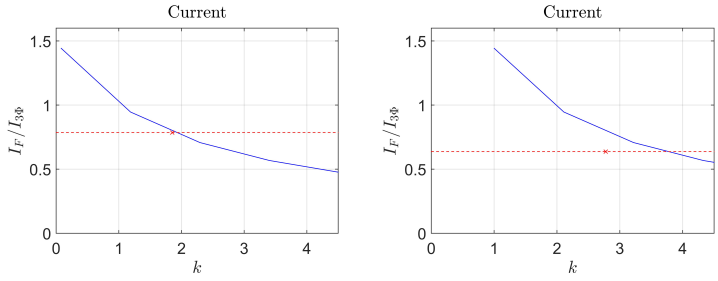

(a) $\mathrm{Dy_n}$-configuration (b) $\mathrm{Y_N y_n}$-configuration

Figure 7.8: Fault current in a GIC immune transformer, the red cross (×) marks the Finnish point, $Z_N = 2.5 + 120i\ \Omega$.

The differing Z_0-values affect the maximum line-to-ground voltage during fault curves as well, Figure 7.9. While the starting k is changed analogously as

for the I_F, the maximum line-to-ground voltage during fault level is the same for a specified k, independent of the configuration.

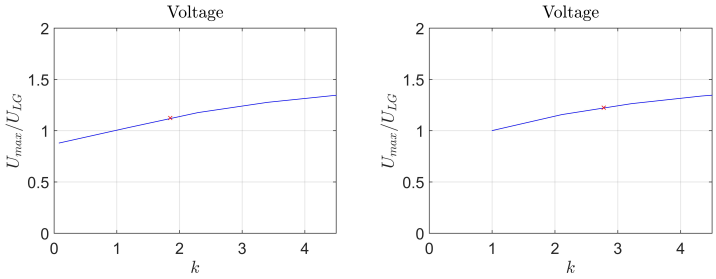

(a) $\mathrm{Dy_n}$-configuration (b) $\mathrm{Y_Ny_n}$-configuration

Figure 7.9: Maximum fault voltage in a regular transformer, the red cross (×) marks the Finnish point, $Z_N = 2.5 + 120i\ \Omega$.

As was the case of the fault current, the maximum line-to-ground voltage during fault in the $\mathrm{Y_Ny_n}$-configuration crosses the Finnish level at a higher k when the compensation winding is connected while there is no noticeable difference in the $\mathrm{Dy_n}$-configuration, Figure 7.10.

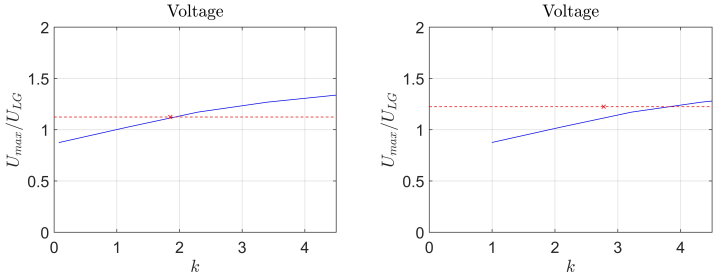

(a) $\mathrm{Dy_n}$-configuration (b) $\mathrm{Y_Ny_n}$-configuration

Figure 7.10: Maximum fault voltage in a GIC immune transformer, the red cross (×) marks the Finnish point, $Z_N = 2.5 + 120i\ \Omega$.

7.3 Summary

The simulations do not exhibit the positive effects of the delta windings mentioned in chapter 2 and seen, when the harmonic magnitude is concerned, in section 4.1 and 4.3. The reason for this is likely limitations in the SimPowerSystem transformer model, since the effect is unmistakably present in the actual system. The effect of using the Finnish Z_N to reduce GIC effects on the transformer is clear though it is apparent that it is not as efficient as the compensation winding in this respect.

In the event of a bolted single-line-to-ground fault, adding the compensation winding has an almost un-noticeable effect on the I_F and maximum line-to-ground voltage during fault (U_{max}) in the $\mathrm{Dy_n}$-connected transformer. This is due to the fact that the setup has a relatively low X_0, the negation of which only alters the characteristics slightly. As the X_0 of the $\mathrm{Y_N y_n}$-connected system has the same order of magnitude as the X_1, negating this, adding the compensation winding, has a notable effect, with higher I_Fs and lower U_{max}s. To achieve the same I_F and U_{max}, a higher k, corresponding to a Z_N approximately $4/3$ the size of the original, is needed.

Chapter 8

Conclusion

8.1 GIC Effects

The presence of Geomagnetically Induced Currents (GICs) is not simple to measure but some effects are easily detected. The experiments and simulations both show that there is a definite correlation between GICs and the second harmonic currents as well as the reactive power losses Q in the transformer. These effects are due to the half-cycle saturation.

In chapter 2 it was mentioned that including a delta winding in the transformer configuration creates a path for a circulating current which prevents the core from being penetrated by the near Direct Current (DC) flux and this means that the transformer saturation and the reactive power loss (Q) is decreased. This effect was confirmed, in regard to the harmonics, by the laboratory experiments though it could not be seen in the simulations. This implies that the simulation model is limited since it does not exhibit the behavior seen in the experiments. The fact that no decrease in Q was found in the lab experiment might be due to the abnormally large resistance in the transformers, reducing the circulating current, though further investigation is needed to establish the cause of this.

The experiments illustrate the significance of core type when it comes to GIC effects, though the dependency is the highest in the three-phase five-legged transformer whereas it should, theoretically, be so in the single-phase transformers. This theoretical dependency was the reason for running the simulations on the single-phase transformers which, in excess of the correlation mentioned above, shows that using the Finnish neutral point impedance (Z_N) decreases the harmonic and Q magnitudes in the system, though not as effectively as the compensation winding.

The GIC immune transformer produced the same results, regardless of core type or connection. This means that the effect of adding the compensation winding is the greatest in the single-phase and five-legged transformers in $\mathrm{Y_N y_n}$-configuration while the impact is less in the three-legged transformer or when a delta winding is present. The magnitude of both the harmonic and Q were equally affected by the compensation winding.

8.2 Fault Behavior

Introducing a single-line-to-ground fault in a system causes a fault current (I_F) to flow and the sound line-to-ground voltages (U_{LG}s) to be altered. The manner in which this happens is determined by the magnitude and type of Z_N, as described in subsection 2.2.2. The experiments display that the I_F is increased and the maximum line-to-ground voltages during fault (U_{max}s) decreased when a grid is connected. This is due to the fact that the grid acts as an alternative path for the current, seen from the fault it is parallel to the transformer. Since the lab transformers had an abnormal zero-sequence reactance to zero-sequence resistance ratio, $^{X_0}/_{R_0}$, the measurements could not be used to draw any further conclusions.

The simulations show that the I_F was higher in the $\mathrm{Dy_n}$- than in the $\mathrm{Y_N y_n}$-configuration of a regular transformer and the opposite applies to the U_{max}s. Adding the compensation winding negates the established zero-sequence reactance (X_0) of the system, which is the sequence parameter that differs the most between the configurations. As an effect of this the I_F and U_{max} values are approximately the same in the two cases. This has a minimal impact on the $\mathrm{Dy_n}$-connected transformer while it is notable in the $\mathrm{Y_N y_n}$-connected case. To achieve the same fault current and maximum line-to-ground voltage during fault levels in the GIC immune version as in the regular the selected Z_N needs to increase the neutral point reactance (X_N) with an amount equivalent to $^1/_3$ the regular X_0, to counteract the negation, since $Z_0 = Z_{0trafo} + 3Z_N$. Because of this the suggestion that a smaller X_N might be usable in combination with the compensation winding is proven false, instead it needs to be $X_{NFinnish} + {}^{X_{0Regular}}/_3$. In these simulations the X_0 is that of the whole setup, not only the transformer, and it is not plausible that all of this should be negated by the compensation winding. If this is actually the case or if it is a consequence of the limitations in the simulation model needs to be investigated. It is, however, worth noting that the Z_N in the GIC immune transformer does not need to have the relatively high DC resistance to attenuate the GICs, i.e. a much higher $^{X_N}/_{R_N}$ can be used, and thus the active power (P) losses could be lowered.

8.3 Summary

The effects of GICs are completely eliminated by the use of the compensation winding. The single-phase and three-phase five-legged core type transformers are much more sensitive to the effects than the three-phase three-legged transformer and connecting one of the windings in a delta configuration significantly decreases the harmonic content, though no effect of this could be seen in regard to the Q losses. Using the patented implementation does not make it possible to use a smaller Z_N while achieving the same fault current and maximum line-to-ground voltage during fault performance, instead the impedance needs to account for the negated X_0 which means that $X_N = X_{NFinnish} + {}^{X_{0Regular}}/_3$.

Chapter 9

Future Work

The simulations in this project were limited to a full scale single-phase transformer setup. Running simulations of the lab setups could be useful in the understanding of limitations in the SimPowerSystem blocks. Furthermore, decreasing the zero-sequence resistance (R_0) and positive-sequence resistance (R_1), so that reasonable $^X/_R$ ratios are obtained, in that model might prove the assumption that the large resistances in the lab transformers were the cause of the uncharacteristic fault behavior. It is also of interest to evaluate the three-phase three-legged and three-phase five-legged transformers in a manner similar to that of the simulations performed on the single-phase transformers in this project. In addition to this, simulations on a more advanced model should provide results closer to the actual power transformers.

Appendix A

Symmetrical Components

Symmetrical components are a powerful technique for analyzing unbalanced three-phase systems developed by Charles Legeyt Fortescue in 1918. It is basically a modeling technique for systematic analysis and design of three-phase systems. There are three components, all consisting of three symmetrical phasors of equal magnitude. In the zero-sequence component the phasors have no phase displacement, in the positive-sequence component they have a $\pm 120°$ phase displacement with a positive sequence and the same goes for the negative-sequence component though in this case the sequence is negative, see Figure A.1 [17].

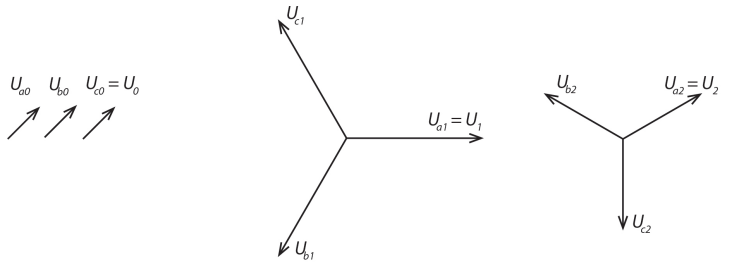

(a) Zero-sequence (b) Positive-sequence (c) Negative-sequence

Figure A.1: Symmetrical component phasors.

For a balanced system the technique generates three separate sequence networks, see Figure A.2, one fore each component, which is advantageous when analyzing the system. For an unbalanced system the sequence networks are connected, but only at the point of unbalance which simplifies the analysis. The phase components, e.g. U_a, U_b and U_c are the values for each phase while the symmetrical components are e.g. zero-sequence voltage (U_0), positive-sequence voltage (U_1) and negative-sequence voltage (U_2) [17].

$$U_p = \begin{bmatrix} U_a \\ U_b \\ U_c \end{bmatrix} \quad U_s = \begin{bmatrix} U_0 \\ U_1 \\ U_2 \end{bmatrix} \tag{A.1}$$

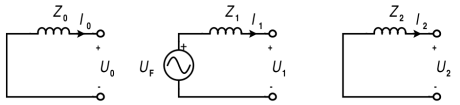

Figure A.2: The sequential networks, zero-, positive- and negative-sequence from left to right.

The linear relationship between the phase components and the symmetrical components is based on the phase shift $a = 1\angle 120°$, which is used to form A and its inverse, A^{-1}.

$$A = \begin{bmatrix} 1 & 1 & 1 \\ 1 & a^2 & a \\ 1 & a & a^2 \end{bmatrix} \tag{A.2}$$

$$A^{-1} = \frac{1}{3}\begin{bmatrix} 1 & 1 & 1 \\ 1 & a & a^2 \\ 1 & a^2 & a \end{bmatrix} \tag{A.3}$$

Once the sequence results are obtained the three-phase equivalents can be easily calculated, see (A.4) [17].

$$\begin{aligned} U_p &= AU_s \\ I_p &= AI_s \end{aligned} \tag{A.4}$$

$$\begin{aligned} U_s &= A^{-1}U_p \\ I_s &= A^{-1}I_p \end{aligned} \tag{A.5}$$

Appendix B

Transformer Parameters

B.1 Per unit base system

The per unit (p.u.) power base (S_{base}) and voltage base (U_{base}) were taken from the transformer specifications and used to calculate the current base (I_{base}), impedance base (Z_{base}) and magnetic flux (ϕ) base (Φ_{base}), see (B.1) and (B.2). The results are shown in Table B.1, the three-phase base applies to both the three-legged and the five-legged transformer.

$$\begin{aligned} I_{base1\Phi} &= \frac{S_{base1\Phi}}{U_{baseLN}} \\ Z_{base1\Phi} &= \frac{U_{baseLN}^2}{S_{base1\Phi}} \\ \Phi_{base1\Phi} &= \sqrt{2}\frac{U_{baseLN}}{2\pi f} \end{aligned} \tag{B.1}$$

$$\begin{aligned} I_{base3\Phi} &= \frac{S_{base3\Phi}}{\sqrt{3}U_{baseLL}} = \frac{S_{base3\Phi}}{3U_{baseLN}} \\ Z_{base3\Phi} &= \frac{U_{baseLL}^2}{S_{base3\Phi}} = \frac{3U_{baseLN}^2}{S_{base3\Phi}} \\ \Phi_{base3\Phi} &= \sqrt{2}\frac{\sqrt{3}U_{baseLL}}{2\pi f} = \sqrt{2}\frac{3U_{baseLN}}{2\pi f} \end{aligned} \tag{B.2}$$

	Single-phase	Three-phase
S_{base} [VA]	800	2400
U_{baseLL} [V]	220	220
U_{baseLN} [V]	127	127
U_{base73} [V]	73	73
U_{base42} [V]	42	42
$I_{basePrim}$ [A]	6.30	6.30
$I_{baseSec}$ [A]	6.30	6.30
I_{base73} [A]	18.89	18.98
I_{base42} [A]	19.05	19.05
$Z_{basePrim}$ [Ω]	20.17	20.17
$Z_{baseSec}$ [Ω]	20.16	20.16
Z_{base73} [Ω]	2.22	2.22
Z_{base42} [Ω]	2.21	2.21
$\Phi_{basePrim}$ [Wb]	0.57	1.72
$\Phi_{baseSec}$ [Wb]	0.57	1.72
Φ_{base73} [Wb]	0.19	0.57
Φ_{base42} [Wb]	0.19	0.57

Table B.1: The per unit (p.u.) bases for the lab transformers.

B.2 Sequence Impedances

The zero- and positive-sequence impedances, (Z_0) and (Z_1), are required in a number of calculations made in this project and since it is the secondary side that is to be examined, it stands to reason that they be determined in reference to this side. To obtain them each transformer type was connected according to Figure B.1 to B.4 in succession. As the figures show the secondary side is Y-connected to the supply and measuring equipment, the National Instruments (NI) devices, while the primary side is either D- or Y-connected, depending on the configuration investigated, [24, 27].

Once the measurements were retrieved a Matlab script determined the complex voltage ($\overline{U}$) and current ($\overline{I}$) from which it calculated Z_0 or Z_1, see (B.3), [25], the results can be found in Table 3.2.

$$\begin{aligned} \overline{Z_0} &= 3\frac{\overline{U_A}}{\overline{I_N}} \\ \overline{Z_1} &= \frac{\overline{U_A}}{\overline{I_A}} \end{aligned} \tag{B.3}$$

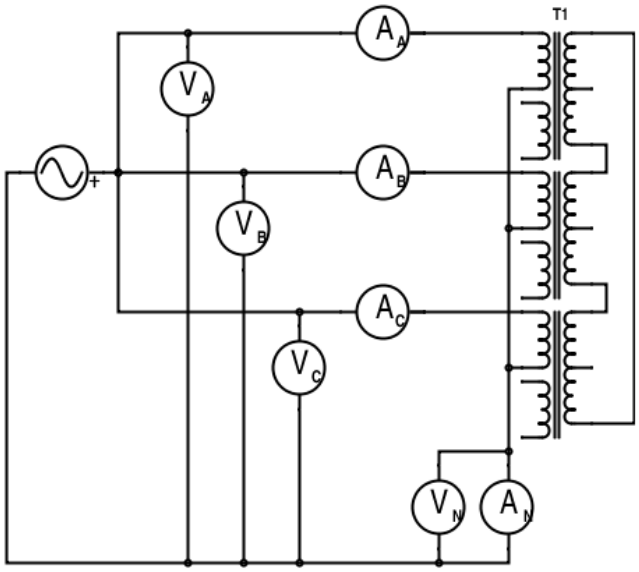

Figure B.1: Schematic for the Dy_n-connected zero-sequence impedance (Z_0) measurement circuit.

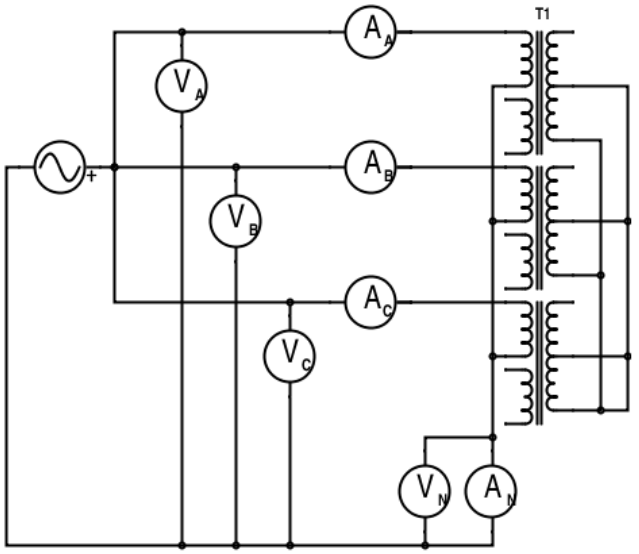

Figure B.2: Schematic for the $Y_N y_n$-connected zero-sequence impedance (Z_0) measurement circuit.

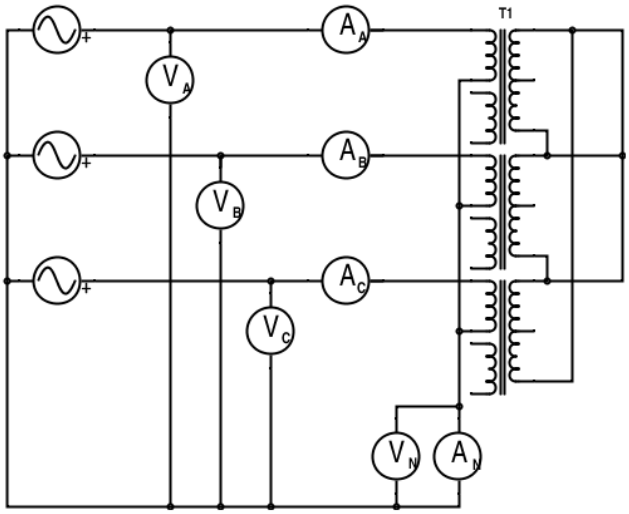

Figure B.3: Schematic for the $\mathrm{Dy_n}$-connected positive-sequence impedance (Z_1) measurement circuit.

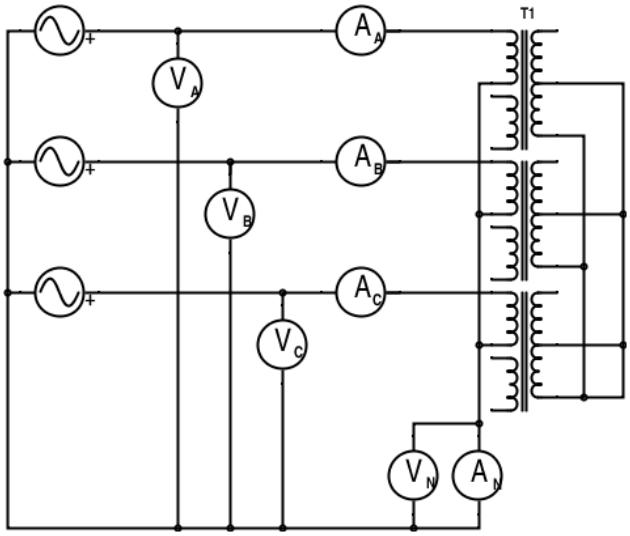

Figure B.4: Schematic for the $\mathrm{Y_N y_n}$-connected positive-sequence impedance (Z_1) measurement circuit.

B.3 Compensation Winding Impedances

In the experiment the three tertiary windings are connected in series and the neutral current is lead through them to compensate the effects of zero-sequence currents (I_0s). Since they are positioned between the neutral point and the grounding impedance they affect the total grounding impedance. For this reason their magnitudes are of interest when comparing the measurement results. These were determined by connecting each transformer according to Figure B.5 and B.6 in turn, closing S_1, tuning the fault current (I_F) to approximately 5.2 A and measuring voltages and currents.

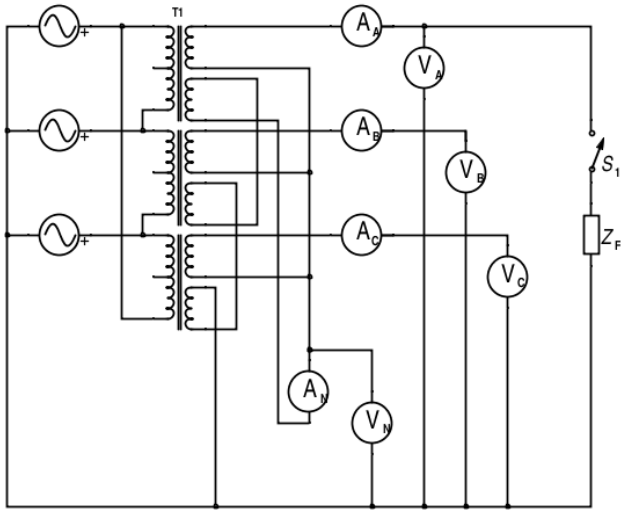

Figure B.5: Schematic for the Dy_n-connected compensation impedance (Z_{comp}) measurement circuit.

As for the sequential impedances, a Matlab script utilized the measurements to determine the complex voltage ($\overline{U}$), current ($\overline{I}$) and calculate Z_{comp} according to (B.4).

$$\overline{Z_{comp}} = \frac{\overline{U_N}}{\overline{I_N}} \tag{B.4}$$

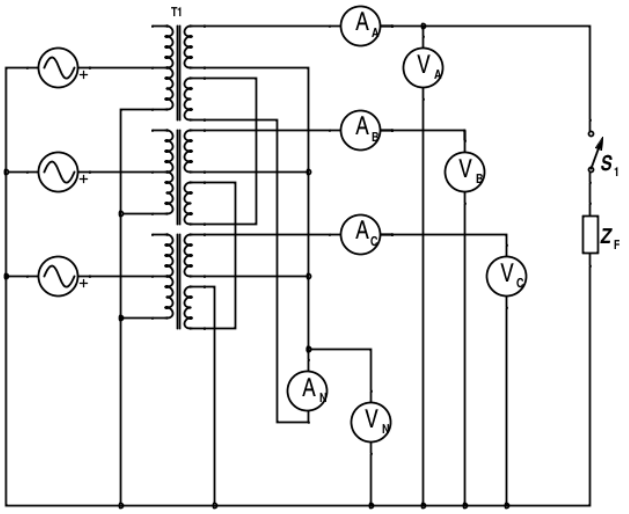

Figure B.6: Schematic for the $Y_N y_n$-connected compensation impedance (Z_{comp}) measurement circuit.

B.4 Magnetization Curve

The saturation characteristics of the transformers is needed to simulate them in the Matlab extension SimPowerSystems. These characteristics were obtained by connecting the transformers according to Figure B.7 or B.8, depending on the configuration, and taking measurements with the NI devices at a line-to-ground voltage of approximately 178 V.

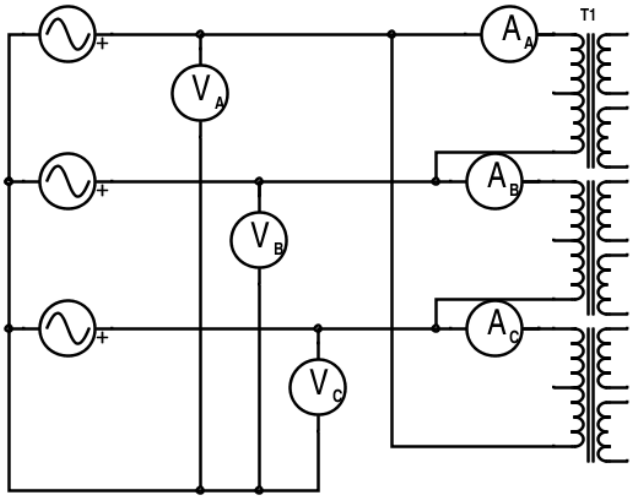

Figure B.7: Schematic for the Dy_n-connected magnetization measurement circuit.

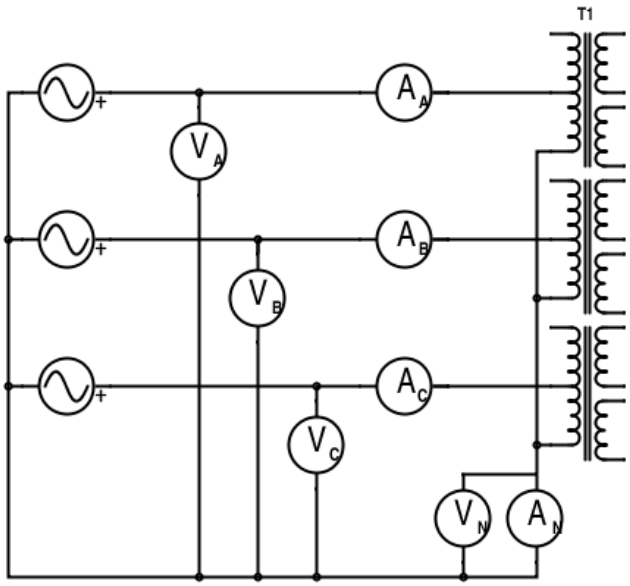

Figure B.8: Schematic for the $Y_N y_n$-connected magnetization measurement circuit.

The measurements were processed by at Matlab script which calculated ϕ, see (B.5), where k is the index of the measurements at hand and h is the time step between samples. The script then converted ϕ to p.u., see (B.6), and plotted the result in reference to the current (i). The curves were approximated with three linear functions each, see Figure B.9 to B.11, and the intersections, origin, and end points give us the characteristics listed Table 3.5.

$$\begin{aligned} \phi_k^* &= \sum_{n=1}^{k} u_n \times h \\ C &= \frac{\max \phi^* - \min \phi^*}{2} \\ \phi_k &= \phi_k^* - C \end{aligned} \tag{B.5}$$

$$\begin{aligned} \phi_{kp.u.} &= \frac{\phi_k}{\Phi_{base}} \\ i_{kp.u.} &= \frac{i_k}{\sqrt{2} I_{base}} \end{aligned} \tag{B.6}$$

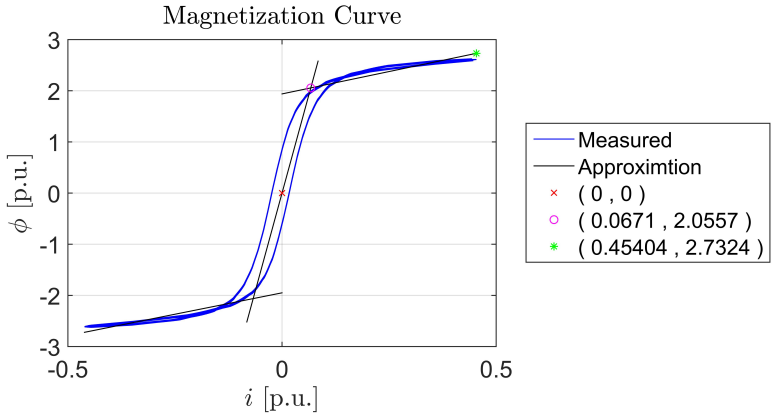

(a) $\mathrm{Dy_n}$-configuration

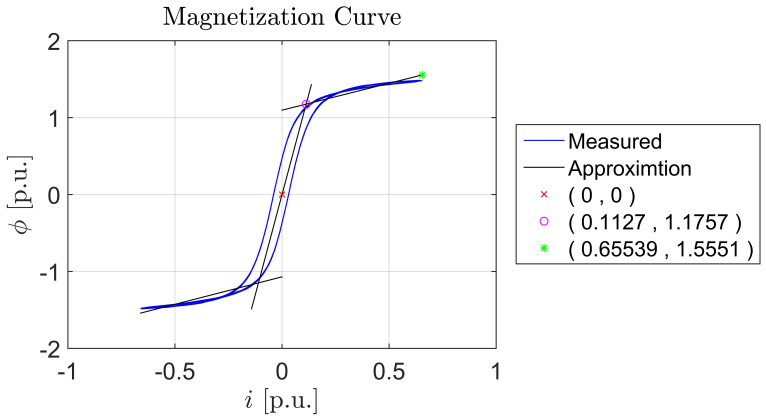

(b) $\mathrm{Y_N y_n}$-configuration

Figure B.9: Magnetization curves for the single-phase transformer.

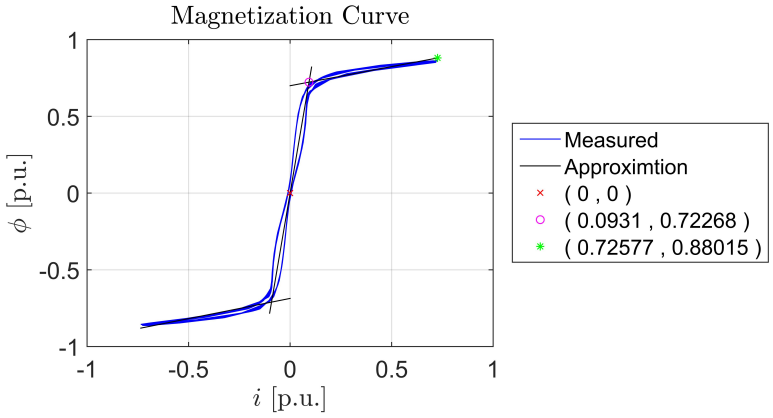

(a) $\mathrm{Dy_n}$-configuration

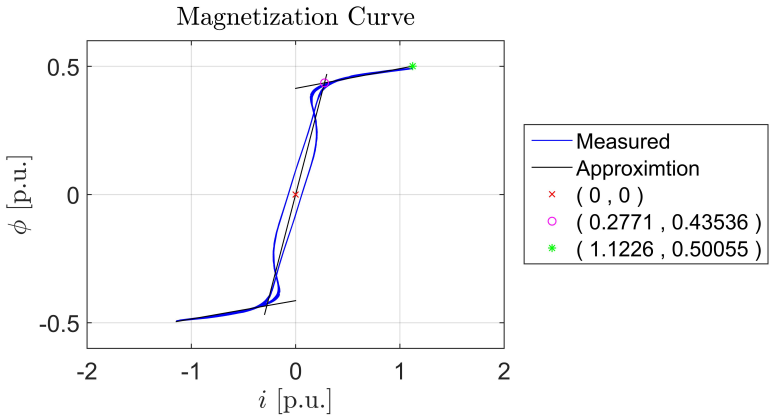

(b) $\mathrm{Y_N y_n}$-configuration

Figure B.10: Magnetization curves for the three-phase three-legged transformer.

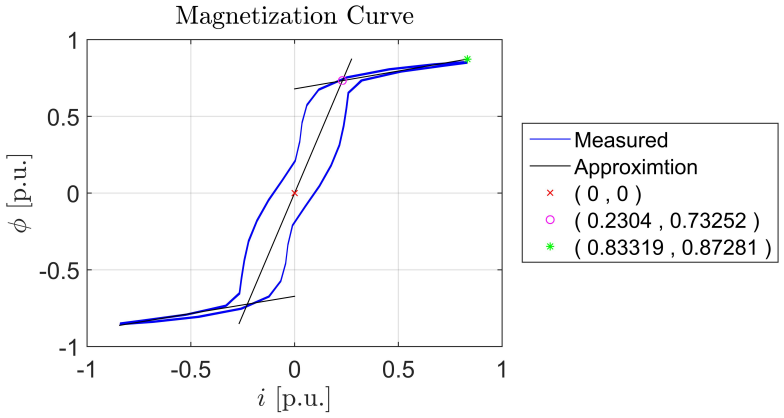

(a) $\mathrm{Dy_n}$-configuration

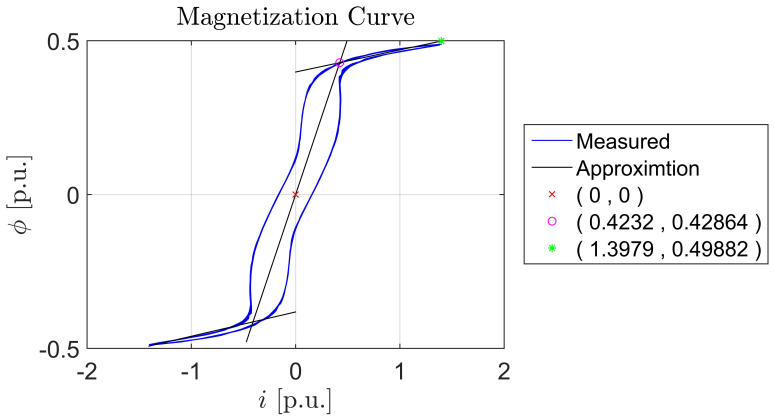

(b) $\mathrm{Y_N y_n}$-configuration

Figure B.11: Magnetization curves for the three-phase five-legged transformer.

B.5 Standard Transformer Test

Parts of the standard transformer test described in [26] were utilized to obtain the parameters needed to simulate the transformers in SimPowerSystems, an extension to Matlab. The measurements in this section were made using the multimeters and wattmeters listed in section 3.2.

A Matlab script was used to calculate all the parameters derived from these tests, Direct Current (DC) resistance (R_{DC}), magnetization resistance (R_m), winding resistance (R_w), magnetization inductance (L_m) and leakage inductance (L_l).

B.5.1 Direct Current Resistance

To determine the R_{DC} each winding was connected according to Figure B.12. The current flow from the car battery was controlled by tuning the 10 Ω potentiometer and set to approximately 1.51 A. Simultaneous reading of the voltage (U_{DC}) and current (I_{DC}) were taken and entered into the Matlab script which calculated the resistance values, using Ohm's Law, both in Ω and in p.u., see (B.7).

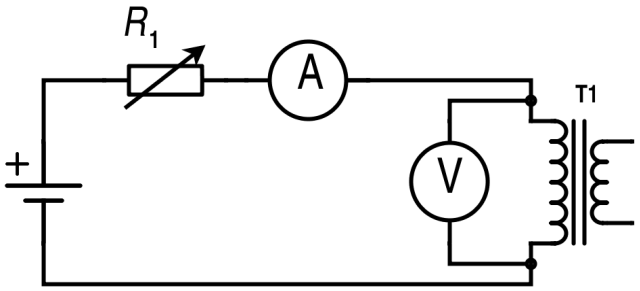

Figure B.12: Schematic for the Direct Current (DC) resistance (R_{DC}) measurement circuit.

$$
\begin{aligned}
R_{DC_i 1\Phi} &= \frac{U_{DC_i}}{I_{DC_i}} \\
R_{DC_i 3\Phi} &= \frac{R_{DC_i A} + R_{DC_i B} + R_{DC_i C}}{3} \\
R_{DC_i p.u.} &= \frac{R_{DC_i}}{Z_{base_i}}
\end{aligned}
\tag{B.7}
$$

B.5.2 No-Load

The no-load test provides the information needed to determine the magnetization parameters, R_m and L_m. One measurement was made for each side and depending on the transformer configuration either the circuit shown in Figure B.13, B.14 or B.15 was used. The voltage was set according to the per unit (p.u.) voltage base (U_{base}) of the connected side and simultaneous reading of the voltage (U_{NL}), current (I_{NL}) and active power (P_{NL}) were made. The

values were inserted in the Matlab script which performed the calculations, see (B.8) to (B.13), needed to obtain R_m and L_m [26, 28].

$$\begin{aligned} S_{NL_i1\Phi} &= U_{NL_i} \times I_{NL_i} \\ S_{NL_i3\Phi} &= 3 \times U_{NL_i} \times I_{NL_i} \\ S_{NL_ip.u.} &= \frac{S_{NL_i}}{S_{base}} \end{aligned} \tag{B.8}$$

$$\begin{aligned} P_{NL_i3\Phi} &= P_{NL_iA} + P_{NL_iB} + P_{NL_iA} \\ P_{NL_ip.u.} &= \frac{P_{NL_i}}{S_{base}} \end{aligned} \tag{B.9}$$

$$\begin{aligned} Q_{NL_i} &= \sqrt{S_{NL_i}^2 - P_{NL_i}^2} \\ Q_{NL_ip.u.} &= \frac{Q_{NL_i}}{S_{base}} \end{aligned} \tag{B.10}$$

$$\begin{aligned} R_{m_i1\Phi} &= \frac{U_{NL_i}^2}{P_{NL_i}} \\ R_{m_i3\Phi} &= \frac{3 \times U_{NL_i}^2}{P_{NL_i}} \\ R_{m_ip.u.} &= \frac{R_{m_i}}{Z_{base}} \\ R_{m_{sum}} &= R_{m_{P220}p.u.} + R_{m_{P127}p.u.} \\ &\quad + R_{m_{S127}p.u.} + R_{m_{T73}p.u.} + R_{m_{T42}p.u.} \\ R_{mp.u.} &= \frac{R_{m_{sum}}}{5} \end{aligned} \tag{B.11}$$

$$\begin{aligned} X_{m_i1\Phi} &= \frac{U_{NL_i}^2}{Q_{NL_i}} \\ X_{m_i3\Phi} &= \frac{3 \times U_{NL_i}^2}{Q_{NL_i}} \\ X_{m_ip.u.} &= \frac{X_{m_i}}{Z_{base}} \\ X_{m_{sum}} &= X_{m_{P220}p.u.} + X_{m_{P127}p.u.} \\ &\quad + X_{m_{S127}p.u.} + X_{m_{T73}p.u.} + X_{m_{T42}p.u.} \\ X_{mp.u.} &= \frac{X_{m_{sum}}}{5} \end{aligned} \tag{B.12}$$

$$\begin{aligned} L_{m_i} &= \frac{X_{m_i}}{2\pi f} \\ L_{m_ip.u.} &= \frac{L_{m_i}}{Z_{base_i}} \\ L_{mp.u.} &= \frac{X_{mp.u.}}{2\pi f} \end{aligned} \tag{B.13}$$

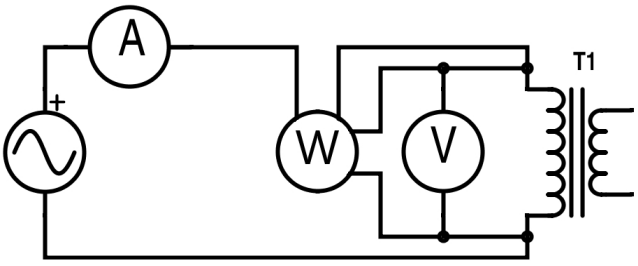

Figure B.13: Schematic for the single-phase no load measurement circuit.

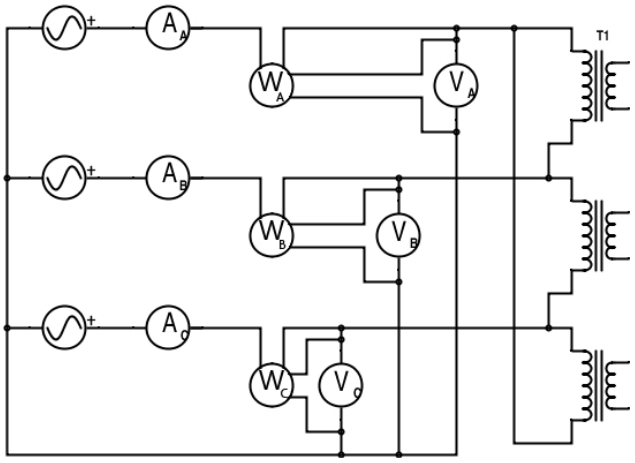

Figure B.14: Schematic for the three-phase Dy_n-connected no load measurement circuit.

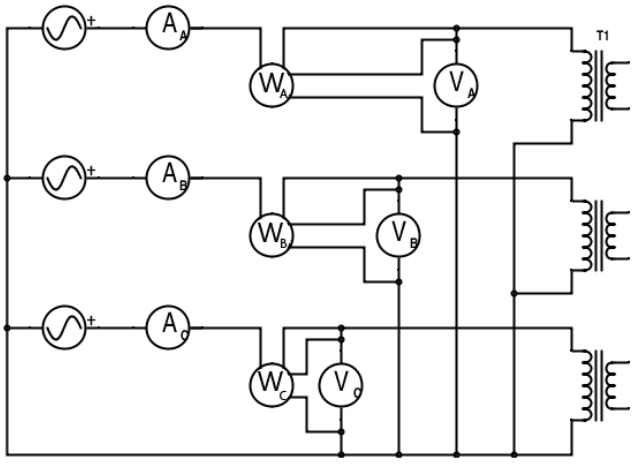

Figure B.15: Schematic for the three-phase $Y_N y_n$-connected no load measurement circuit.

B.5.3 Short-Circuit

In order to determine the values of R_w and L_l short-circuit tests were performed. One measurement was made for each combination of sides and depending on the transformer configuration either the circuit shown in Figure B.16, B.17 or B.18 was used. The voltage was tuned to obtain a 5.2 A current and simultaneous reading of the voltage (U_{SC}), current (I_{SC}) and active power (P_{SC}) were made. The values were inserted in the Matlab script which performed the calculations, see (B.14) to (B.19), needed to obtain R_w and L_l [26, 28].

$$\begin{aligned} R_{k_{i,j}1\Phi} &= \frac{P_{SC_{i,j}}}{I^2_{SC_{i,j}}} \\ R_{k_{i,j}3\Phi} &= \frac{P_{SC_{i,j}}}{3 \times I^2_{SC_{i,j}}} \end{aligned} \tag{B.14}$$

$$\begin{aligned} R_{w_{i,j}} &= \frac{R_{k_{i,j}}}{1 + \left(\frac{U_i}{U_j}\right)^2} \\ R_{w_P} &= \frac{R_{w_{P,S}} - R_{w_{S,T}} + R_{w_{T,P}}}{2} \\ R_{w_S} &= \frac{R_{w_{S,T}} - R_{w_{T,P}} + R_{w_{P,S}}}{2} \\ R_{w_T} &= \frac{R_{w_{T,P}} - R_{w_{P,S}} + R_{w_{S,T}}}{2} \\ R_{w_i p.u.} &= \frac{R_{w_i}}{Z_{base_i}} \end{aligned} \tag{B.15}$$

$$Z_{k_{i,j}} = \frac{U_{SC_{i,j}}}{I_{SC_{i,j}}} \tag{B.16}$$

$$X_{k_{i,j}} = \sqrt{Z^2_{k_{i,j}} - R^2_{k_{i,j}}} \tag{B.17}$$

$$\begin{aligned} X_{l_{i,j}} &= \frac{X_{k_{i,j}}}{1 + \left(\frac{U_i}{U_j}\right)^2} \\ X_{l_P} &= \frac{X_{l_{P,S}} - X_{l_{S,T}} + X_{l_{T,P}}}{2} \\ X_{l_S} &= \frac{X_{l_{S,T}} - X_{l_{T,P}} + X_{l_{P,S}}}{2} \\ X_{l_T} &= \frac{X_{l_{T,P}} - X_{l_{P,S}} + X_{l_{S,T}}}{2} \\ X_{l_i p.u.} &= \frac{X_{l_i}}{Z_{base_i}} \end{aligned} \tag{B.18}$$

$$
\begin{aligned}
L_{l_i} &= \frac{X_{l_i}}{2\pi f} \\
L_{l_i p.u.} &= \frac{L_{l_i}}{Z_{base_i}}
\end{aligned}
\tag{B.19}
$$

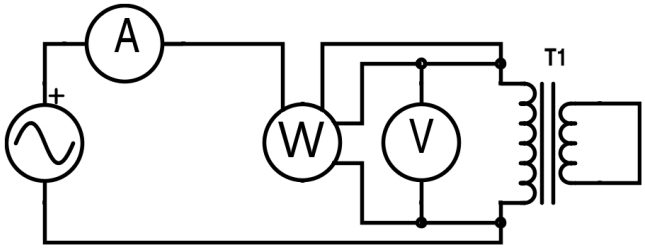

Figure B.16: Schematic for the single-phase short-circuit measurement circuit.

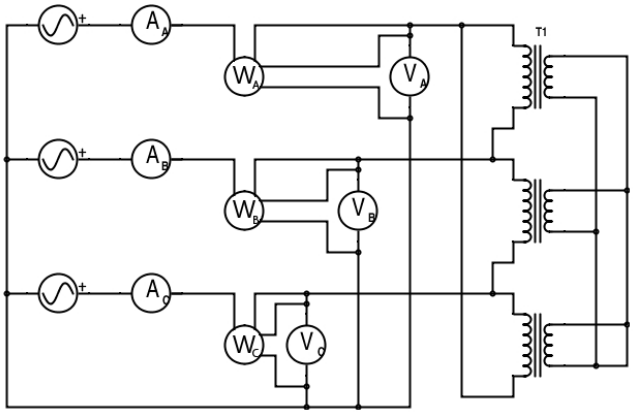

Figure B.17: Schematic for the three-phase $\mathrm{Dy_n}$-connected short-circuit measurement circuit.

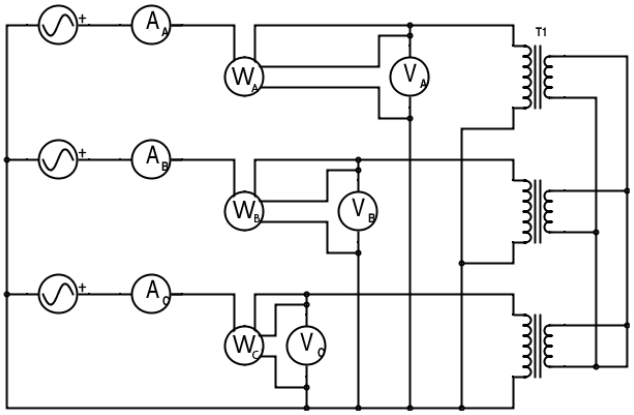

Figure B.18: Schematic for the three-phase $Y_N y_n$-connected short-circuit measurement circuit.

Appendix C

Disctrete Fourier Transform

A simplified view on Fourier transform is that it can be used to describe the frequency content of a signal as the sum of sinusoidal functions. A Discrete Fourier Transform (DFT) can thus be applied to a series of sampled measurements for the same purpose. By selecting certain settings, e.g. using a sampling frequency which results in an even number, N, of samples being taken during one period of the measured signal, the DFT expression can be simplified. With these specifications it follows that $N/2 - 1$ harmonics can be determined. The p:th harmonic is derived according to (C.1), where y_n is the current value in the series, [25, 29].

$$\begin{aligned} \theta &= \frac{2\pi}{N} \\ \overline{Y_p} &= \frac{2}{N} \sum_{n=1}^{N} y_n e^{-ipn\theta} \end{aligned} \tag{C.1}$$

Bibliography

[1] M. AF Klercker Alaküla and S. Lindahl, "Transformer with protection against direct current magnetization caused by zero sequence current," 2008, uS Patent 7,432,699.

[2] T. S. Molinski, "Why utilities respect geomagnetically induced currents," *Journal of atmospheric and solar-terrestrial physics*, vol. 64 (16), pp. 1765–1778, 2002.

[3] R. Pirjola, "Averages of geomagnetically induced currents (GIC) in the Finnish 400kV electric power transmission system and the effect of neutral point reactors on GIC," *Journal of Atmospheric and Solar-Terrestrial Physics*, vol. 67, no. 7, pp. 701 – 708, 2005. [Online]. Available: http://ludwig.lub.lu.se/login?url=http://search.ebscohost.com/login.aspx?direct=true&db=inh&AN=8583418&site=eds-live&scope=site

[4] O. Samuelsson, "Power transformer immune to geomagnetically induced currents," in *Power and Energy Society General Meeting (PES), 2013 IEEE*, IEEE. IEEE, July 2013, pp. 1–5.

[5] R. J. Pirjola and D. H. Boteler, "Geomagnetically induced currents in european high-voltage power systems," in *Electrical and Computer Engineering, 2006. CCECE '06. Canadian Conference on.* IEEE, May 2006, pp. 1263–1266.

[6] ESA and NASA. (2013, April) Our star the sun. [Online]. Available: http://soho.esac.esa.int/classroom/classroom.html

[7] H. E. J. Koskinen, *Physics of Space Storms: From the Solar Surface to the Earth.* Springer, 2011.

[8] B. T. Tsurutani and W. D. Gonzalez, "The causes of geomagnetic storms during solar maximum," *Eos Trans. AGU*, vol. 75(5), pp. 49–53, 1994.

[9] P. N. Mayaud, *Derivation, Meaning, and Use of Geomagnetic Indices.* American Geophysical Union, 1980.

[10] A. Banerjee, A. Bej, and T. Chatterjee, "On the existence of a long range correlation in the geomagnetic disturbance storm time (dst) index." *Astrophysics and Space Science*, vol. 337, no. 1, pp. 23 – 32, 2012. [Online]. Available: http://ludwig.lub.lu.se/login?url=http://search.ebscohost.com/login.aspx?direct=true&db=inh&AN=13317172&site=eds-live&scope=site

[11] A. Rezaei-Zare, "Behavior of single-phase transformers under geomagnetically induced current conditions," *Power Delivery, IEEE Transactions on*, vol. 29 (2), pp. 916–925, April 2014.

[12] IEEE Power & Energy Society Technical Council Task Force on Geomagnetic Disturbances, "Geomagnetic disturbances: Their impact on the power grid," *Power and Energy Magazine, IEEE*, vol. 11 (4), pp. 71–78, July-August 2013.

[13] National Academy of Sciences, *Severe Space Weather Events - Understanding Societal and Economic Impacts: A Workshop Report - Extended Summary.* National Academies Press, Washington, D.C., 2009. [Online]. Available: http://www.nap.edu/catalog.php?record_id=12643

[14] M. Lahtinen and J. Elovaara, "Gic occurrences and gic test for 400 kv system transformer," *Power Delivery, IEEE Transactions on*, vol. 17 (2), pp. 555 – 561, April 2002.

[15] H. Zhu and T. J. Overbye, "Blocking device placement for mitigating the effects of geomagnetically induced currents," *Power Systems, IEEE Transactions on*, 2014.

[16] J. D. Glover, M. S. Sarma, and T. Overbye, *Power System Analysis & Design, SI Edition*, 5th ed. Cengage Learning, 2011, ch. 9, pp. 471–515.

[17] ——, *Power System Analysis & Design, SI Edition*, 5th ed. Cengage Learning, 2011, ch. 8, pp. 419–470.

[18] D. J. Keen, "Not our fault! - earth faults, past, present and future and their mitigation." Cigré, Tech. Rep., 9 2013. [Online]. Available: http://www.slideshare.net/den15nz/223-not-our-fault-earth-faults-past-present-and-future-and-their-mitigation-d-j-keen?from_action=save

[19] S. Lindahl, "Neutral and system earthing," 2001.

[20] ——, "Modern power system protection grounding of distribution circuits," 2003.

[21] "IEEE Guide for the Application of Neutral Grounding in Electrical Utility Systems - Part 1: Introduction," *IEEE Std C62.92.1-2000*, pp. i–25, 2001.

[22] A. J. Pesonen, J. Maaskola, and J. Elovaara, "Special features of earth-fault currents," in *High currents in power systems*, CIGRE. Imatran Voima Oy, 1985.

[23] R. Roeper, F. Mitlehner, B. Ehmcke, and A. Webs, *Short-circuit currents in three-phase systems.* Siemens, 1985.

[24] O. Evenson, "Kompendium i reläteknik för högspänningsanläggningar - Del 2: Inställning och provning (in Swedish)," Kungliga Vattenfallsstyrelsen, 1961.

[25] A. Christensson and E. Lingärde, "Transformatorers beteende vid fasavbrott i matande spänning (in Swedish)," Master's thesis, Division of Industrial Electrical Engineering and Automation, Faculty of Engineeting, Lund University, 2014. [Online]. Available: http://iea.lth.se/publications/pubmsc.html

[26] "IEEE Standard Test Code for Liquid-Immersed Distribution, Power, and Regulating Transformers and IEEE Guide for Short-Circuit Testing of Distribution and Power Transformers," *ANSI/IEEE Std C57.12.90-1987*, pp. 1–82, 1988.

[27] E. Sorrentino and J. Burgos, "Comparison of methods for measuring zero sequence impedances in 3-phase core-type transformers," in *Universities Power Engineering Conference (UPEC), 2012 47th International*, Sept 2012, pp. 1–5.

[28] Department of Industrial Electrical Engineering and Automatio, Lund Institute of Technology, Ed., *Elmaskinsystem (in Swedish).* KF-Sigma Lund, 1995, ch. 6, pp. 124–127.

[29] J. S. Thorp and A. G. Phadke, *Control and Dynamic Systems V41: Analysis and Control System Techniques for Electric Power Systems Part 4 of 4: Advances in Theory and Applications.* Elsevier, 2012, vol. 41, ch. 1 - Computer Relaying in Power Systems, pp. 23–25.

Index

Numbers written in italic refer to the page where the corresponding entry is described; numbers underlined refer to the definition; numbers in roman refer to the pages where the entry is used.